Bulletin of Volcanology (2025) 87:75
https://doi.org/10.1007/s00445-025-01862-9

RESEARCH ARTICLE

Magma source, pre-eruptive dynamics and timescales of major explosions at Stromboli volcano (Italy)

Laura Insinga[1] · Marija Voloschina[2] · Paola Marianelli[2] · Erika Bartolomeo[2] · Antonella Bertagnini[3] · Nicole Métrich[4] · Silvio G. Rotolo[1,5] · Alessandro Aiuppa[1] · Maurizio Ripepe[6] · Marco Pistolesi[2,3]

Received: 14 March 2025 / Accepted: 4 August 2025

Abstract

At Stromboli volcano (Italy) the regular, persistent activity is occasionally (2–4 events/year) interrupted by sudden, short-lived and more energetic major explosions, being intermediate in size between regular Strombolian activity and even more powerful paroxysmal explosions. Despite being frequent and hazardous, the magma source depth, the triggering mechanisms and timescales of such major explosions are still poorly understood. Here, we focus on three major explosions which occurred on 3 May, 8 November and 24 November 2009. We present a dataset of major element composition and dissolved volatile contents in olivine-hosted melt inclusions, embayments and glassy groundmass. We combine them with Fe–Mg diffusion profiles in olivine phenocrysts, and with volcanic gas plume and ground tilt measurements. Olivine phenocrysts display $Fo_{69\text{-}72}$ compositions, with reverse zoning (up to Fo_{83}) in the 24 November and to a minor extent in the 8 November eruption. Glassy groundmass of the November events ranges from the more evolved towards more primitive compositions, whereas the 3 May 2009 glassy groundmass has evolved compositions. Dissolved H_2O and CO_2 in glassy and bubble-free melt inclusions are low, with CO_2 below the detection limit and H_2O up to 2.3 wt.%. Volcanic plume measurements indicate the occurrence of these events in phases of high CO_2 fluxes, with substantial geochemical changes preceding the onset of the 24 November event. Based on these results, we propose that the 3 May major explosion — the smallest in intensity/magnitude — was likely driven by the accumulation of gas bubbles into the shallower (< 1 km below sea level, b.s.l.) HP reservoir. In contrast, we find the November major explosions to be triggered by the injection of variable amounts of deeper-stored LP magma and gas into the HP reservoir, over hours to weeks before.

Keywords Explosive basaltic eruptions · Stromboli · Major explosions · Melt inclusions · Olivine · Volcanic plume chemistry

Editorial responsibility: M. Edmonds

✉ Laura Insinga
laura.insinga@unipa.it

[1] MareDipartimento di Scienze della Terra e del Mare, Università di Palermo, Palermo, Italy

[2] Dipartimento di Scienze della Terra, Università di Pisa, Pisa, Italy

[3] Istituto Nazionale Di Geofisica E Vulcanologia, Sezione Di Pisa, Pisa, Italy

[4] Institut de Physique du Globe de Paris, Université Paris-Cité, CNRS, Paris, France

[5] Istituto Nazionale di Geofisica e Vulcanologia, Sezione di Palermo, Palermo, Italy

[6] Dipartimento di Scienze della Terra, Università di Firenze, Florence, Italy

Introduction

Basaltic, open-vent volcanoes are prominent sources of volcanic gases into the atmosphere (Carn et. al. 2016; Edmonds et al. 2022), and produce a wide spectrum of explosive eruptions, varying in scale and style from low-intensity Strombolian eruptions to paroxysmal events of Vulcanian to Plinian magnitude (e.g., Houghton and Gonnermann 2008; Allard 2010; Vergniolle and Métrich 2021; Barth et al. 2024; Vergniolle 2024).

Stromboli, located at the north-easternmost edge of the Aeolian archipelago (Southern Italy) (Fig. 1a), is one of these open-vent volcanoes (Aiuppa et al. 2021; Métrich et al. 2021; Ripepe et al. 2021), having been characterized by open-vent conditions at least since the seventh century CE (Rosi et al. 2013).

Published online: 22 August 2025

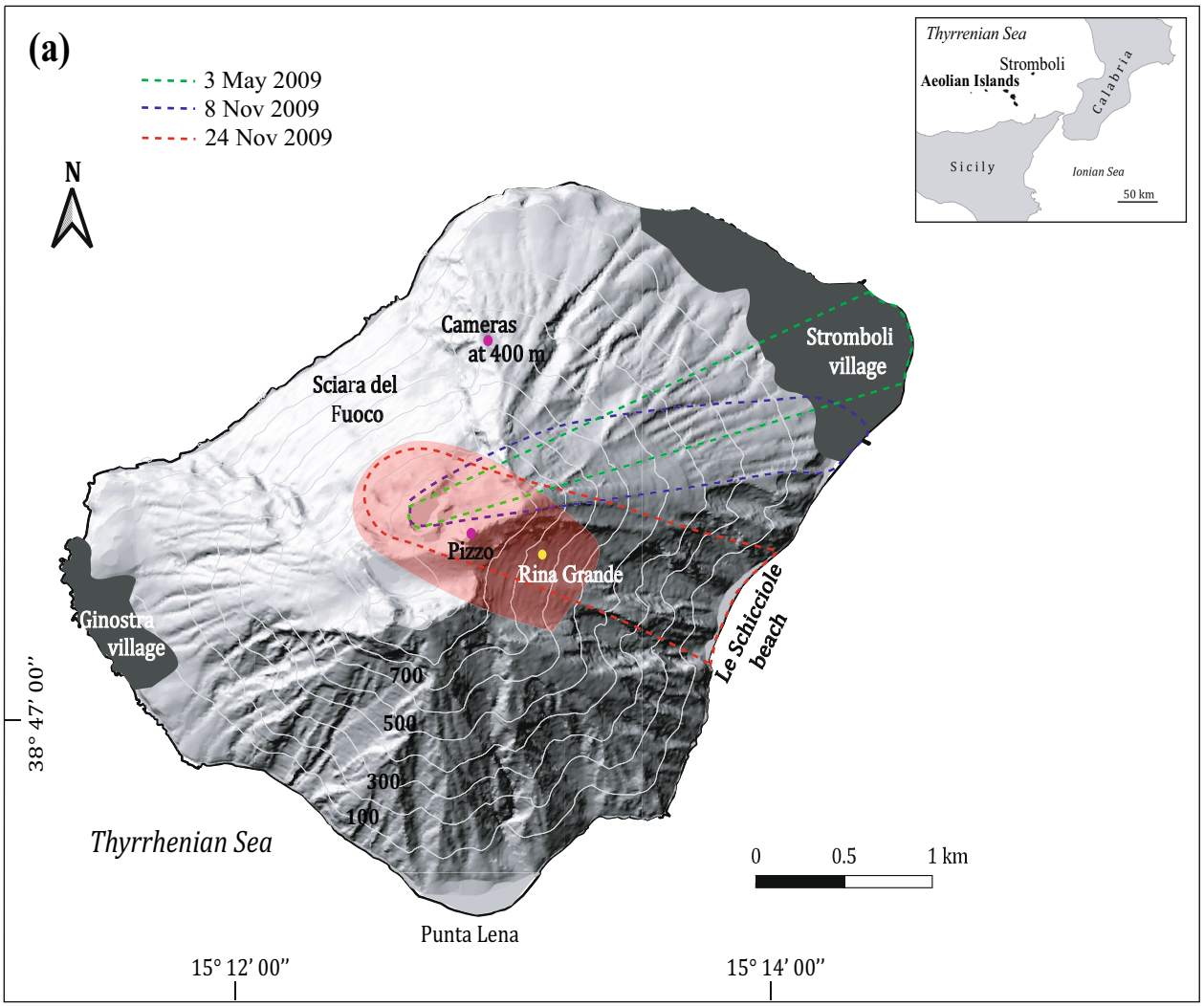
(a)
3 May 2009
8 Nov 2009
24 Nov 2009
N
Thyrrenian Sea
Stromboli
Aeolian Islands
Calabria
Sicily
Ionian Sea
50 km
Cameras
at 400 m
Sciara del
Fuoco
Stromboli
village
Pizzo
Rina Grande
Ginostra
village
Le Schicciole
beach
700
500
300
100
Thyrrhenian Sea
0
0.5
1 km
38° 47' 00''
Punta Lena
15° 12' 00''
15° 14' 00''


(b)


(c)


(d)

◂**Fig. 1** **a** Shaded relief map of Stromboli Island showing the tephra dispersal of the 3 May, 8 November and 24 November 2009 major explosions (dashed green, blue and red lines, respectively), the location of video-cameras and of the main localities. Red area indicates the area affected by spatters and bombs during the 24 November major explosion. Data of products dispersion are taken from Andronico (2009) for the 3 May 2009 and from Andronico and Pistolesi (2010) for the 8 and 24 November 2009 major explosions. **b** 3 May, **c** 8 November and **d** 24 November 2009 eruptive products. Note the mingled bomb showing the black scoriaceous HP and the LP pumiceous components

Its persistent explosive dynamics is characterized by rhythmic, mild to moderate Strombolian explosions, known as *ordinary activity*. These explosions repeat every 10–20 min on average, last a few seconds, and eject pyroclastic material up to heights of 100–200 m (Ripepe et al. 2008; Taddeucci et al. 2012; Kelfoun et al. 2020). Tephra volumes are typically ~ 1–10 m^3, with mass discharge rates of 10^2–10^3 kg/s (Rosi et al. 2013 and references therein). Such regular explosive activity is preceded by a ~ 150 s long, low-amplitude (~ 0.1 μrad) inflation of the ground and is followed by a rapid deflation (~ 30 s) (Genco & Ripepe 2010; Ripepe et al. 2021).

This steady activity is occasionally interrupted by sudden, more violent and short-lived (tens of seconds to few minutes) explosions often involving multiple vents simultaneously and ranging in intensity and magnitude from *major explosions* to *paroxysms* (Barberi et al. 1993; Bertagnini et al. 2011). The last paroxysms occurred in 2003, 2007, 2019 and 2024 (Métrich et al. 2005, 2010, 2021; Andronico et al. 2021; Giordano and De Astis 2021) — they are highly energetic (mass discharge rate > 10^6 kg/s; Rosi et al. 2006, 2013; Pistolesi et al. 2011; Pioli et al. 2014) explosions and produce eruptive plumes rising to 3–8 km above the crater terrace (Pioli et al. 2014) or up to 10 km in the larger-scale events (e.g., 22 May 1919 or 11 September 1930; Ponte 1919; Rittman 1931). Paroxysms are associated with the ejection of bombs and meter-sized ballistic blocks at distances up to 2.5 km from the vents. These more violent events are preceded by longer (up to 600 s) and larger (~ 10 μrad) ground deformation compared to the ordinary activity.

Extensive geochemical and petrological research has been conducted on pyroclastic materials erupted at Stromboli, finding diverse compositional signatures for ordinary activity and paroxysms.

Ordinary activity is fed by a crystal-rich (~ 50 vol.%) and partially degassed (H_2O < 0.6 wt.%, CO_2 < 100 ppm, S < 1300 ppm, Cl < 2700 ppm) basaltic-shoshonitic magma (K_2O = 1.9–2.5 wt.%; SiO_2 = 48.5–51.5 wt.%), emitted as a high-porphyritic (HP) black scoria. The mineral assemblage consists of phenocrysts of plagioclase (An_{60-90}), clinopyroxene ($Mg\#_{0.70-0.90,}$ Fs_{5-17}), olivine (Fo_{70-74}), all set in a shoshonitic glassy groundmass (K_2O > 3.8 wt.%; Bertagnini et al. 2008; Francalanci et al. 2004; Métrich et al. 2001, 2010; Landi et al. 2004, 2008, 2022).

In contrast, paroxysms are fed by a volatile-rich basaltic magma (H_2O = 1.8–3.4 wt.%; CO_2 = 890–1890 ppm; S = 1660–2250 ppm; Cl = 1660–2030 ppm) straddling the high-K (HK) shoshonitic field. This is erupted as crystal-poor (< 10 vol.%) and low-porphyritic (LP) golden pumices. Mineralogy consists of clinopyroxene ($Mg\#_{0.84-0.90}$, Fs_{5-8}) and olivine with predominant composition Fo_{85-86} in small-scale paroxysms (e.g., 15 March 2007, 3 July 2019) and Fo_{88-91} in the larger-scale paroxysms (e.g., 11 September 1930), set in a shoshonitic-basaltic, vesicle-rich glassy groundmass (K_2O < 2.4 wt.%; Bertagnini et al. 2003, 2008; Francalanci et al. 2004; Landi et al. 2004, 2009, 2022; Métrich et al. 2001, 2005, 2010, 2021).

Based on these evidence, previous studies have inferred the existence of a complex, vertically extended plumbing system.

The ordinary activity is caused by the surface bursting of gas slugs, formed by the coalescence of smaller bubbles within the upper conduit (< 3 km b.s.l.; Burton et al. 2007) resident HP magma.

Paroxysms instead have been recognized to have a deeper source, and are triggered by the interplay of several processes including (i) the intrusion of hot and CO_2-rich bubbly magma causing pressurization of the deep volcano's plumbing system (7–11 km b.s.l.) (Métrich et al. 2001, 2005, 2021; Bertagnini et al. 2003, 2008; Francalanci et al. 2004; Pichavant et al. 2011), (ii) collapse and fast ascent of a deeply accumulated CO_2-rich foam, previously stored at the roof of the LP reservoir (Allard 2010; Aiuppa et al. 2011, 2021) or at some rheological discontinuity (Caricchi et al. 2024).

Based on eruptive parameters, paroxysms can be also separated in two main categories (Large-scale –LSP– and Small-scale –SSP– paroxysms), which in turn reflect slight variability of magmatic source region and compositional characteristics (Bertagnini et al. 2008, 2011; Métrich et al. 2005, 2010, 2021; Pistolesi et al. 2011; Rosi et al. 2013).

Constraints on the timescales of paroxysms are given by Fe–Mg diffusion profiles in olivine crystals and suggest magma ascent times of 2–10 days from 6 to 9 km to the surface, and long (months) incubation times for destabilization of the LP magma reservoir (Métrich et al. 2021). These timescales are in agreement with timescales derived from plume gas measurements (Aiuppa et al. 2021).

In contrast to ordinary activity and paroxysms whose magma sources, pre-eruptive dynamics and timescales are relatively well constrained, much less is known on the triggering mechanisms of major explosions.

Here, we present a petrological and geochemical study of three major explosions of variable intensity occurred on 3 May, 8 November and 24 November 2009, with the aim of

reconstructing their pre-eruptive dynamics and their timescales from the deep storage level to ascent to surface. To this aim (i) we retrieve the pre-eruptive storage conditions by measuring dissolved volatiles contents (H_2O, CO_2, S, Cl) in olivine hosted melt inclusions, accompanied by analysis of major and minor element of their host olivine crystals, and (ii) we constrain the timescales of pre-eruptive processes by modelling Fe–Mg compositional profiles in zoned olivine crystals.

Source and dynamics of major explosions: state of the art

Major explosions are sporadic (2 events/year; Barberi et al. 1993; Bertagnini et al. 2008; Bevilacqua et al. 2020) eruptions of intermediate size (Pioli et al. 2014). They produce plumes a few hundred metres in height (Bertagnini et al. 2003; Andronico et al. 2008) forming discontinuous blankets of tephra deposits sporadically reaching the coastline, and a shower of bombs and meter-sized lithic blocks covering the upper slopes of the volcano, typically to maximum distance of ~ 1.5 km from the vents.

The ejected tephra volumes are typically in the 10^2–10^3 m^3 range, with mass discharge rates of 10^4–10^5 kg/s (Rosi et al. 2013; Pioli et al. 2014). These mid-intensity events are preceded by smaller (~ 1 μrad) ground deformation compared to paroxysms, starting ~ 300 s before the onset of the eruption. Nevertheless, they are characterized by similar deformation trends (Ripepe et al. 2021).

Major explosions are characterized by a heterogeneity of their eruptive products. The lowest-intensity explosions produce exclusively HP scoria (e.g., 8 September 1998; Bertagnini et al. 1999), as well as the ordinary activity. The higher intensity events (3 May, 8 November, 24 November 2009; La Felice and Landi 2011) are instead complex mixtures of both HP scoria and LP pumices, also showing intermediate glassy groundmass composition in between.

In addition to the heterogeneity of their eruptive products, interpretation is additionally complicated by the under-sampling of these events, which deposits are poorly dispersed and usually not long preserved.

A relatively deeper source origin than ordinary activity is supported by the gas observations (Aiuppa et al. 2021) that recorded gas plume CO_2/SO_2 ratios above background in six major explosions occurred between 2018 and 2020, including the 19 July 2020 event. Geophysically, this event exhibited a ground tilt ~ 4 times higher than the average for major explosions (3.5 μrad vs. 0.8 μrad), thus ranking at the boundary between major explosions and small-scale paroxysms (Ripepe et al. 2021).

Voloschina et al. (2023) used H_2O and CO_2 compositions measured in olivine-hosted melt inclusions to constrain the magma source of this peculiar major explosion to be at ~ 9.5 km b.s.l. depth with the activation of a shallower (5–6 km b.s.l.) ponding zone. Based on Fe–Mg diffusion profiles in olivine crystals, they suggested shorter incubation (20–25 days before the onset) with longer ascent times (5–10 days) than those associated to paroxysms. However, it is currently unknown if similar triggering/incubation depths and timescales also apply to other, less energetic, major explosions.

The 2009 major explosions at Stromboli

Three major explosions hit Stromboli on 3 May, 8 November and 24 November 2009, with the latter event being the most energetic since the 2007 paroxysm for erupted volume, pyroclastic tephra dispersal and recorded amplitude of syn-eruptive seismic and infrasonic signals as recorded by the various monitoring networks deployed on the island (Andronico and Pistolesi 2010; Aiuppa et al. 2011).

The 3 May 2009 event was preceded by deformation of the summit crater area since 20 March 2009 as detected by ground-based interferometric synthetic aperture radar (Nolesini et al. 2013). This ground deformation episode reached a maximum of 0.35 mm/h on 27 March 2009 and remained high for the following month until 3 May 2009, when it was 0.25 mm/h. INGV (Istituto Nazionale di Geofisica e Vulcanologia) reported a first explosion at 14:58:08 GMT (Cristaldi 2009a) from the central sector of the crater terrace, producing the emission of coarse pyroclasts that reached a height of 200 m above the crater rim, and then fell mostly within the crater terrace but also outside its NW sector, and was followed by a terminal ash emission. As observed from visible and thermal cameras, a second larger explosion occurred at 14:58:28 GMT from the southern vent, radially ejecting metric-sized dark spatter bombs over the whole field of view of a camera installed on the summit area at Pizzo (Fig. 1a). The eruptive plume generated a shower of ash and lapilli in ENE direction, eventually reaching the village of Stromboli and forming a discontinuous tephra deposit that was partially washed away by a violent storm the day after (Andronico 2009). Lava fountaining and ash emission were observed to follow the main event from other vents. An intense spattering activity started at 15:00 GMT and produced a small intracrateric lava flow (Andronico 2009). The monitoring network of LGS (Laboratorio di Geofisica Sperimentale – University of Florence, Italy n.d.) recorded an associated seismic, very-long-period (VLP) amplitude of 7 μm, a ground deformation of ~ 0.8 μrad and an infrasonic pressure of ~ 5 bar, thus classifying the 3 May 2009 event as a major explosion.

After the 3 May event, a new increase in the deformation rate at the summit crater area started on 2 November

2009 (0.56 mm/h) as recorded by the ground-based interferometric synthetic aperture radar and reached 0.6 mm/h on 8 November 2009 (Nolesini et al. 2013) when, at 12:29:31 GMT, a mild explosion (column height, ~ 50 m) occurred at the central crater (Cristaldi 2009b). This produced the fallout of coarse, incandescent materials and was followed by two main explosions of lapilli and ash, that lasted about 38 s. Tephra was dispersed ENE within a distance of 2.5 km from the vents, covering a dispersal area on the ground of around 10,000 m^2 (Andronico and Pistolesi 2010). Intense lava fountaining from the southern sector started at 12:30:25 and lasted 50 s, followed by 20 min of intense continuous spattering from the central sector. The activity was accompanied for 5 min by the effusion of an intracrateric lava and was classified as a major explosion. The LGS monitoring network recorded a seismic velocity and displacement of 8×10^{-4} m/s and 3×10^{-5} m, respectively, 6 bar of infrasonic pressure and a ground deformation of 0.57 μrad.

After 8 November, activity returned to background levels but on 24 November 2009, another major explosion occurred at 11:20:48 GMT, consisting of simultaneous bursts from two active vents located in the southern sector of the crater associated with a recorded ground deformation of 0.61 μrad recorded by the LGS network. A ~ 150 m eruptive plume generated ash to lapilli fallout, also ejecting proximal bombs and lava fragments from a central, previously inactive vent. A second, more intense explosion followed after 15 s that radially ejected a larger volume of juvenile bombs and lithic clasts, affecting the whole summit area at least 300 m from the vent. The eruptive plume emplaced tephra fallout over the summit area and in particularly in the Pizzo sopra la Fossa area and towards E reaching the shoreline at the Schicciole beach, 1.6 km SE from eruptive vent (Fig. 1a). Several fires were ignited by tephra fallout in the eastern sector of the island below Rina Grande. The second explosion produced a 50 m wide crater in the central sector of the crater terrace, where a following intense degassing and spattering were observed. The total sequence lasted 50 s and produced a larger dispersal and volume of tephra compared to the other two major explosions, covering an area of 15,000 m^2 (Andronico and Pistolesi 2010).

Sample preparation and analytical methods

Criteria of sample selection and description

Samples were collected by D. Andronico and M. Pistolesi few days after each explosive event (see Andronico and Pistolesi 2010 for details). Mingled pumices were crushed and sieved in the 1–0.5 mm and 0.5–0.25 mm granulometric fractions. Olivine crystals were hand-picked under a binocular stereomicroscope and were embedded in orthodontic resin. A total of 57 melt inclusions (MIs) and 3 embayments were selected and doubly polished in order to expose both sides, except some exceedingly thin (< 10 μm) melt inclusions that were exposed only on one side.

Melt inclusions were found to be more abundant in olivine relative to pyroxene or plagioclase crystals; we hence selected and analysed exclusively those hosted in olivine crystals. Olivine-hosted melt inclusions have sizes ranging from 20 to 180 μm in diameter, and show variable morphologies: well-rounded, ellipsoidal, faceted (negative host crystal shapes), squared and irregularly shaped (Fig. 2a–c; Fig. S1 in Supplementary Figures).

After their entrapment, melt inclusions may be affected by modifications in response to changing T-P-X-fO_2 magma conditions, including crystallization of the host mineral at the host-inclusion interface and exsolution of volatiles into a bubble (shrinkage bubble), that can significantly deplete CO_2 in the melt due to its low solubility (Anderson and Brown 1993; Dixon and Stolper 1995; Métrich and Wallace 2008; Wallace et al. 2015a,b; Rose-Koga et al. 2021). The majority (48/57) of melt inclusions analysed in this study is entirely glassy, whereas a minority contain mineral daughters (4/57) or bubbles (3/57); relatively to these latter, bubble volumes are all in the usual range of shrinkage bubbles (0.2 to 5 vol% of the melt volume; Lowenstern 1995; Steele-MacInnis et al. 2017), excluding the heterogeneous trapping of a mixture consisting of gas and melt mixture.

A description of analysed melt inclusions and host olivine crystals, from each eruptive event, is reported in Table S1 (Supplementary Material 1) detailing location of melt inclusions in olivine crystals (core/rim), size, shape, eventual presence and size of bubbles and/or daughter minerals. Embayments and glassy groundmass wetting the olivine phenocrysts were also analysed.

Fourier-transform infrared spectroscopy

Fourier-transform infrared spectroscopy (FTIR) was conducted at the Dipartimento di Scienze della Terra of the University of Pisa (Italy) using a Nicolet iN10 FTIR Microscope equipped with a global infra-red source and a Ge-coated KBr beamsplitter, in order to analyse dissolved volatiles (H_2O, CO_2) in melt inclusions, embayments and glassy groundmass. For spot analyses, a liquid-nitrogen cooled MCT detector was used, and the aperture varied from 11 to 33 μm square, depending on inclusion size. In larger melt inclusions, several spectra were acquired using different sizes to verify the consistency of aperture size, in agreement with the recommendations of Rose-Koga et al. (2021). Spectra were acquired in the 400–6000 cm^{-1} absorption range, collecting 512 scans at a resolution of 8 cm^{-1} for glasses and 256 scans for olivine crystals and background. The beam path within the microscope

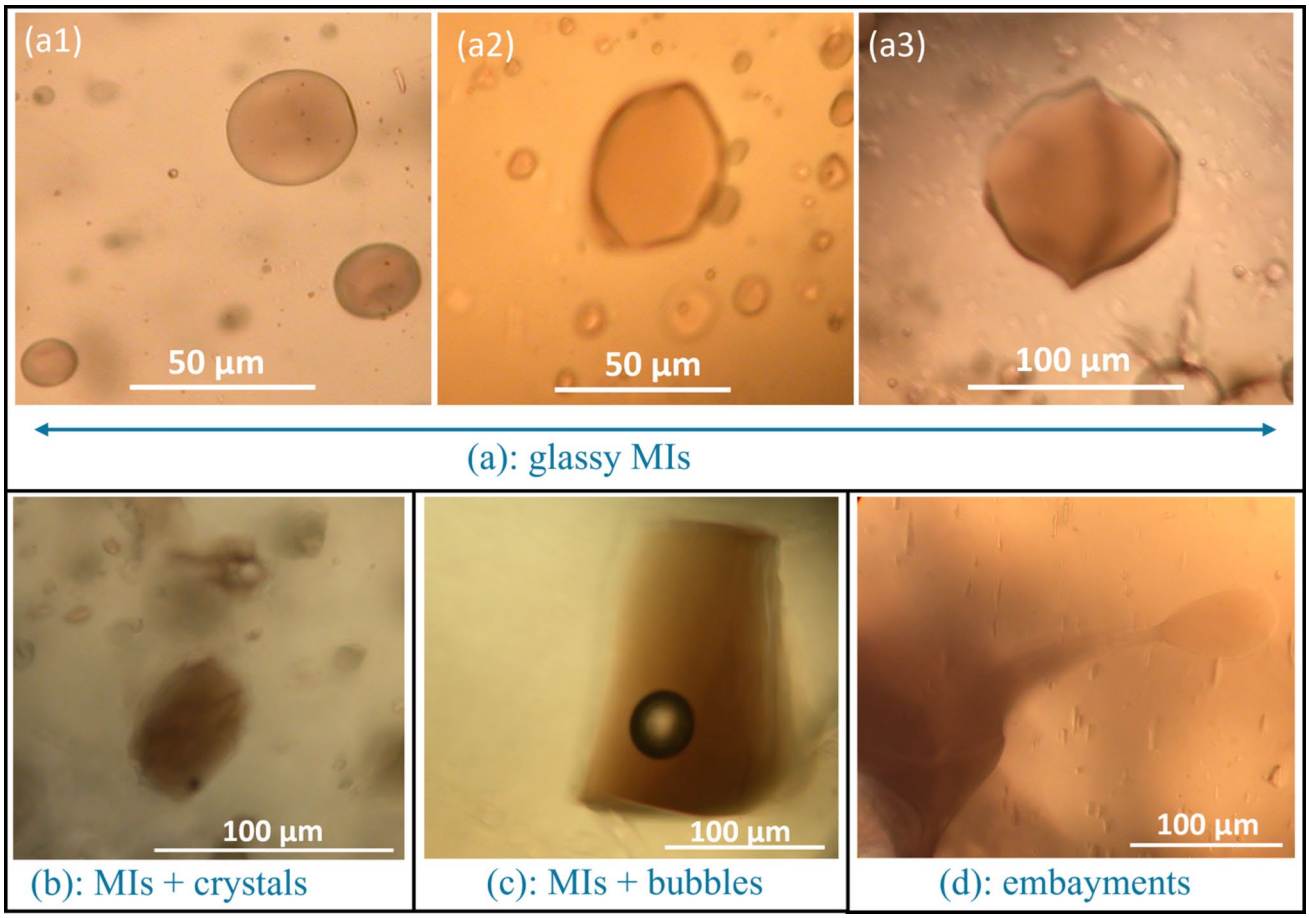

Fig. 2 Transmitted light microphotographs of olivine-hosted melt inclusions with various morphologies: (a): glassy melt inclusions; (a1): well-rounded (a = b axis), glassy melt inclusions; (a2) faceted, large melt inclusion; (a3) squared melt inclusion; (b): melt inclusion with mineral daughters; (c): melt inclusion with a 40 µm shrinkage bubble; (d) melt embayment

was continuously purged with a continuous flux of dry, CO_2-free compressed air with a − 73 °C dewpoint. The software Omnic Picta was used to control the microscope's imaging and FTIR capabilities.

H_2O and CO_2 concentrations were calculated according to the Beer-Lambert law:

$$C = \frac{100 \times Abs \times M}{\varepsilon \times \rho \times t}$$

where Abs is the absorbance, M the molar mass (g/mol), ε the extinction coefficient (L/mol per cm), ρ the glass density, and t the thickness (cm). Water absorption was calculated by measuring the total H_2O absorption band centred at a wavenumber of 3535 cm^{-1} using a straight baseline correction, while the CO_3^{2-} peak doublet was collected at 1520 cm^{-1} and 1430 cm^{-1}. CO_2 peak deconvolution was carried out through Peak Fit software after the subtraction of a degassed glass spectrum obtained from measurements of the glassy groundmass. The partially exposed melt inclusions and embayments were corrected for olivine crystal spectra, by measuring olivine absorption between 1600 and 2000 cm^{-1} in both the glass and in the host mineral spectra (Von Aulock et al. 2014). Density used is an averaged value (2.69 ± 0.02 g/cm^3), determined on Stromboli hydrous glasses (Métrich et al. 2001). Extinction coefficients (ε) were: $\varepsilon^{3535} = 64.3$ L/mol per cm (Métrich et al. 2001) and $\varepsilon^{1520} = 362$ L/mol per cm (Voloschina et al. 2023). Olivine thickness (t) was previously measured with a calibrated microscope stage at magnifications of 10× and 50×. Multiple measurements were taken at different spots along the crystals and an average thickness was then calculated for individual crystals. Analytical uncertainties in H_2O and CO_2 concentrations were calculated based on propagation of error from wafer thickness, determining a maximum error of 13%. Given that H_2O and CO_2 solubilities are strongly dependent on pressure, under the assumption that melt inclusions were vapor-saturated at the time of entrapment, the use of a H_2O-CO_2 solubility model (i.e., Newman and Lowenstern 2002; Iacono-Marziano et al. 2012; Ghiorso and Gualda 2015; Shishkina et al. 2014) allowed calculating their

saturation pressures (P_{sat}) and, thus, to retrieve the magmatic storage depth (e.g., Métrich and Wallace 2008; Wallace et al. 2021). Calculations were done in VESIcal 1.0.1 (Iacovino et al. 2021), using a JupyterLab computing environment hosted on the ENKI server (http://enki-portal.org/).

Electron microprobe analyses

Samples previously analysed by FTIR and additional olivine crystals were embedded in epoxy resin and then carbon coated for microanalysis. Major element, S and Cl composition of glasses (melt inclusions, embayments and glassy groundmass) and olivine crystals were obtained by electron microprobe analysis (EPMA) at the joint laboratory (LaMA) of the DST and CNR-IGG of Firenze (Italy) using a JEOL Superprobe JXA-8230 equipped with 5 wavelength dispersion spectrometers (WDS). Glasses and olivine crystals from 3 May 2009 were analysed at the Unitech COSPECT at the University of Milan, Italy, using a JEOL 8200 Super Probe. Analyses on olivine crystals were performed using an accelerating voltage of 15 kV, a beam current of 20 nA and a beam diameter of 3 µm. Glass analyses were performed at 15 kV, 10 nA, using a defocused beam diameter of 5 to 10 µm. ZAF correction for matrix effects was applied. Different counting times were set for major and minor elements: 15 s on peak and 7 s on background for major elements, 30–40 s on peak and 15–20 s for minor elements, excluding Na. To reduce alkali loss, Na was measured first, for 10 s on peak and 5 on background. The relative elemental average errors were obtained from counting statistics and were found to be ≤ 2% for Mg, ≤ 2% for Fe, 1% for Ca, Al and K, ≤ 3% for Na, 5% for Cl (9% for the 3 May products) and 27% for S (the latter increasing in analyses of the glassy groundmass). The analytical standards used for calibration were basaltic glasses from SE Indian ocean (NMNH 113716–1, NMNH 111240–52). Analytical errors and accuracy of electron microprobe analyses are reported in Table S11-15 (Supplementary Material 3).

In the larger melt inclusions, several spot analyses were collected and then averaged. A total of 63 spot analyses were collected on the glassy groundmass, but specifically on the 3 May 2009 clasts, the low amount of the LP component did not allow a detailed analysis of its glassy groundmass and crystals. Olivine composition was analysed in multiple spots close to MIs and in the rims of host crystals, for a total of 240 spot analyses collected. Due to the double polishing procedure often leaving only olivine fragments, additional olivine phenocrysts were selected, oriented and mounted in epoxy resin for collecting Fe–Mg diffusion profiles, obtaining a total of 15 concentration profiles. Diffusion profiles were positioned following the suggestions of Shea et al. (2015).

Post-entrapment crystallization and melting

Post-entrapment crystallization (PEC) and melting (PEM) were calculated by using the Melt Inclusion Modification Correction (MIMiC) program (Rassmussen et al. 2020), which calculates the olivine-melt equilibrium Fe–Mg distribution coefficient ($Kd^{Fe-Mg}_{ol-melt}$) using the model of Toplis (2005), then adding incrementally olivine composition to the melt inclusion until equilibrium Kd is reached.

Post-entrapment crystallization (PEC) of olivine mainly affects MgO, FeO and SiO_2, which are compatible in olivine, whereas incompatible elements (e.g. volatile elements) could suffer a potential increase only if the amount of PEC is > 5% (Rose-Koga et al. 2021). The amount of PEC required for the analysed MIs is < 5.5 wt.% (Table S2, Supplementary Material 1; Fig. S10 in Supplementary Figures). Melt inclusions may also undergo post-entrapment melting due to overheating (Sobolev and Kostyuk 1975; Rasmussen et al. 2020), but this effect is limited in our case (1.5 wt.% on average; Table S2, Supplementary Material 1). Considering that both PEC and PEM values are negligible and that ratios such as CaO/Al_2O_3 and K_2O/Na_2O, as well as H_2O, CO_2 and S would be diluted to a similar degree, in the following not-recalculated compositions are considered.

Fe–Mg timescales

A total of 10 out of 15 Fe–Mg concentration profiles in olivine phenocrysts (6 from the 24 November and 4 from the 8 November 2009) were modelled by using the Diffusion Process Analysis (DIPRA) software (Girona and Costa 2013), in order to calculate timescales of pre-eruptive magmatic processes.

The orientation of olivine crystals was carried out by visual inspection of the crystal shape under an optical microscope.

Pre-eruptive conditions were fixed at 1085 °C (± 37 °C) and 76 MPa. The chosen temperature represents an average of values calculated using the geothermometer of Putirka et al. (2007) on 14 melt inclusions from this study. Although it is lower than the 1150 °C temperature used for Fe–Mg diffusion calculation for the 2020 major explosion and for paroxysms (Voloschina et al. 2023; Métrich et al. 2021), it still falls within the lower temperature range (1050–1175 °C) derived from experimental studies conducted on a LP basalt pumice of Stromboli (Di Carlo et al. 2006). The pressure value of 76 MPa was chosen in order to simulate the shallow magmatic reservoir of Stromboli, in accordance with the lower pressure bound (50–100 MPa) reported by Di Carlo et al. (2006). The redox conditions were fixed at NNO + 1 (NNO refers to the Ni-NiO oxygen buffer), in line with previous studies (e.g., Aiuppa et al. 2010; Métrich et al. 2021; Voloschina et al. 2023) and representative of the oxidizing

conditions of the Stromboli magmas. Natural concentration profiles were modelled considering non-homogeneous and step initial conditions. Input parameters used in DIPRA are reported in Table S10 (Supplementary Material 2).

Volcanic gas

Volcanic gas data were obtained from daily survey of the plume flux of Stromboli volcano carried out during the 2006–2010 years. Specifically, the CO_2 plume flux was determined by simultaneous measurements of the CO_2/SO_2 plume ratio by three fully automated Multi-GAS instruments and SO_2 mass flux was determined by a remotely controlled network consisting of four UV scanning DOAS spectrometers (see Aiuppa et al. 2011 for further details and for location of the MultiGAS and UV scanner stations).

Results

Major element data

Groundmass composition

Glassy groundmass from the 24 November 2009 samples ranges from shoshonitic ($K_2O = 2.08–2.48$ wt.%; $SiO_2 = 48.71–50.80$ wt.%) to shoshonitic-basaltic ($K_2O = 3.59–3.94$ wt.%; $SiO_2 = 49.83–51.83$ wt.%) (Fig. S2 in Supplementary Figures), in agreement with previous results reported in La Felice and Landi (2011). These compositions cluster both in the fields of LP ($K_2O < 2.4$ wt.%) and HP ($K_2O > 3.8$ wt.%) magmas, respectively (Landi et al. 2022). The high variability in K_2O contents likely suggests mixing between magma batches having slightly variable melt and mineral compositions (Voloschina et al. 2023). This is further observable in Fig. 3 and 4 where major element ratios exhibit a wide variability ($K_2O/Na_2O = 0.77–1.20$; $CaO/Al_2O_3 = 0.48–0.67$), spanning from a more evolved composition ($K_2O/Na_2O > 1$; $CaO/Al_2O_3 < 0.5$) to the compositional fields of the April 2003 and March 2007 small-scale paroxysms (SSP; Métrich et al. 2005, 2010) and historic large-scale paroxysms (LSP; Métrich et al. 2010).

For comparison, the glassy groundmass of the 19 July 2020 major explosion (Voloschina et al. 2023) shows a similar compositional trend. The 24 November 2009 glassy groundmass is Fe-richer ($FeO = 7.77–9.77$ wt.%; $MgO = 3.58–5.83$ wt.%; $FeO/MgO = 1.44–2.70$) than the groundmass of 19 July 2020 ($FeO = 7.32–8.97$ wt.%; $MgO = 4.21–7.68$ wt.%; Voloschina et al. 2023). The glassy groundmass of the 8 November 2009 eruption shows intermediate compositions, from shoshonitic basalt toward the shoshonitic basaltic field straddling with the HK basalt field ($K_2O = 2.23–4.06$ wt.%; $MgO = 3.49–7.45$ wt.%;

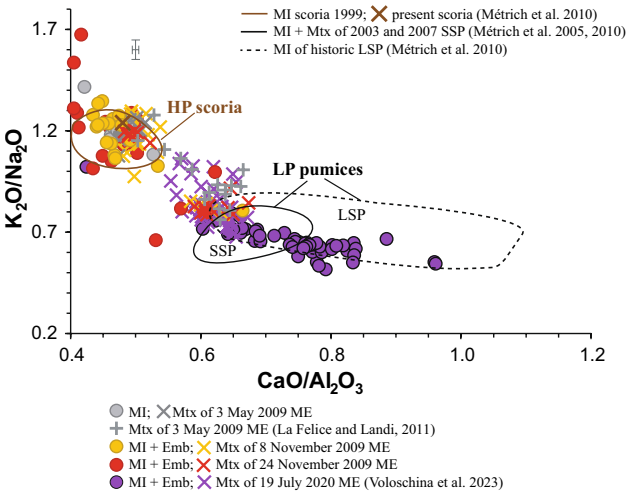

Fig. 3 K_2O/Na_2O vs CaO/Al_2O_3 ratios of melt inclusions (MIs), embayments (Emb) and glassy groundmass (Mtx) from different Stromboli eruptions: 1999 scoria (ordinary activity, Métrich et al. 2010); 3 May 2009 (this study; La Felice and Landi 2011), 8 November 2009 (this study) and 24 November 2009 (this study) major explosions (ME); 19 July 2020 major explosion (Voloschina et al. 2023); 2003 and 2007 small-scale paroxysms (SSP; Métrich et al. 2005, 2010); historic large-scale paroxysms (LSP; Métrich et al. 2010). Filled dots represent melt inclusions and/or embayments, cross symbols represent glassy groundmass. Average errors ($K_2O/Na_2O = 3\%$ and $CaO/Al_2O_3 = 1\%$) are indicated as error bars. HP, high porphyritic; LP, low porphyritic

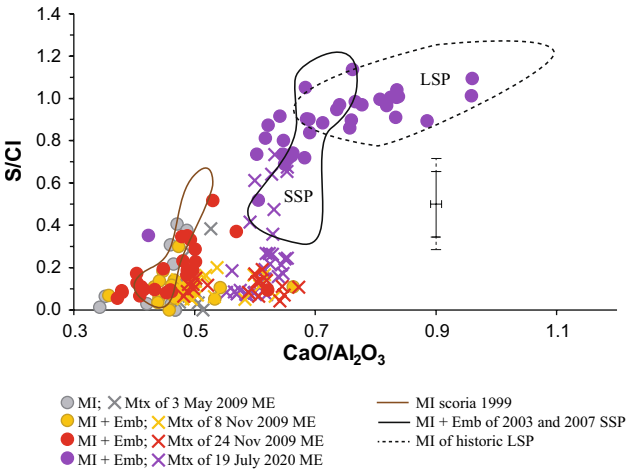

Fig. 4 S/Cl vs CaO/Al_2O_3 ratios of melt inclusions, embayments and glassy groundmass from different eruptions at Stromboli: 1999 scoria (ordinary activity, Métrich et al. 2010); 3 May 2009, 8 November and 24 November 2009 major explosions (ME; this study); 19 July 2020 major explosion (Voloschina et al. 2023); 2003 and 2007 small-scale paroxysms (SSP; Métrich et al. 2005; 2010); historic large-scale paroxysms (LSP; Métrich et al. 2010). Filled dots represent melt inclusions (MI) and/or embayments (Emb), crosses represent glassy groundmass (Mtx). Average errors (S/Cl = 31% for MI/Emb and 43% for Mtx; $CaO/Al_2O_3 = 1\%$) are indicated as error bars: solid bar indicates MI and Emb errors, dashed bar indicates Mtx error

SiO_2 = 48.06–52.09 wt.%) (Fig. S2 in Supplementary Figures). Glassy groundmass of the 3 May 2009 eruption is shoshonitic-basaltic in composition (K_2O = 3.78–4.04 wt.%; MgO = 3.39–3.88 wt.%, SiO_2 = 49.89–53.64 wt.%) and plots in the HP compositional field (Fig. 3, K_2O/Na_2O = 1.08–1.27; CaO/Al_2O_3 = 0.47–0.51).

Melt inclusions and embayments

Major element ratios in melt inclusions and embayments of the 24 November 2009 (K_2O/Na_2O = 0.66–1.67; CaO/Al_2O_3 = 0.37–0.62) mostly overlap the HP magma compositions, except few MIs that have intermediate compositions close to the LP compositional field. Melt inclusions and embayments are even Fe-richer (FeO = 9.05–12.73 wt.%; MgO = 2.62–3.99 wt.%; FeO/MgO = 2.51–4.52) than associated groundmass and melt inclusions from July 2020 (FeO = 5.93–9.17 wt.%, MgO = 1.94–5.52; Voloschina et al. 2023), 5 April 2003 (FeO = 7.43–9.09 wt.%; MgO = 4.99–6.78 wt.%; Métrich et al. 2005), and 15 March 2007 (FeO = 7.49–8.43 wt.%, MgO = 4.85–5.12 wt.%; Métrich et al. 2010). According to Bertagnini et al. (2003), Fe-rich melt inclusions could derive from the entrainment and dissolution of pre-existing Fe-richer olivine crystals into melts of different differentiation degree, with successive crystallization and possible post-entrapment re-equilibration. Generally, composition of glasses is comparable but more evolved than whole-rock compositions of the same eruption (MgO = 6.07–6.02 wt.%, CaO = 11.21–11.46; La Felice and Landi 2011).

Major elements ratios in melt inclusions of the 8 November 2009 (K_2O/Na_2O = 0.79–1.30, CaO/Al_2O_3 = 0.47–0.63) cover the entire range from the HP toward the LP compositional fields (Fig. 3). Compositions cluster in and around the HP compositional field (K_2O/Na_2O = 1.03–1.50, CaO/Al_2O_3 = 0.36–0.53), except for one MI overlapping with the LP field (K_2O/Na_2O = 0.66, CaO/Al_2O_3 = 0.66). Melt embayments show comparable compositions of K_2O/Na_2O = 1.06–1.24 and CaO/Al_2O_3 = 0.44–0.47. Melt inclusions and embayments are Fe-rich (FeO = 8.52–11.49 wt.%), with values comparable to melt inclusions of 3 May 2009.

Melt inclusions of the 3 May 2009 event (CaO/Al_2O_3 = 0.34–0.53; K_2O/Na_2O = 1.08–1.61) also plot in the HP compositional field and are slightly less Fe-rich than the 24 November melt inclusions (FeO = 8.12–11.08 wt.%). Our studied glassy groundmasses of 3 May 2009 are compositionally more evolved than whole-rocks (MgO = 6.07 wt.%, CaO = 11.36 wt.%; La Felice and Landi 2011).

Olivine composition and Fe–Mg diffusion profiles

We selected olivine crystals mostly belonging to the 0.5–1 mm fraction size and few to the 250–500 µm fraction, with morphologies varying from tabular to euhedral and no difference being evident between the two size fractions.

Two main populations (A and B) of olivine crystals were identified in the samples of the 3 major explosions:

- Group A comprises variably reverse-zoned olivine crystals that constitute the most abundant population (76% of the total); these can be further subdivided into subgroup A1, with more pronounced reversely-zoned olivine crystals with Fo_{69-71} cores and Fo_{76-83} rims, and subgroup A2 that are slightly reversely zoned olivine crystals with Fo_{69-71} cores and Fo_{72-73} rims. Olivine crystals belonging to these two subsets contain abundant melt inclusions mostly clustering in the core and in some cases have developed a variably thick (50–100 µm), Mg-rich reaction rim (Fig. 5c).

- Group B consists of olivine phenocrysts (24%) that are compositionally homogeneous (Fo_{70-71}) and bear a single, large melt inclusion (Fig. 6a).

Olivine crystals from the 8 November 2009 are mostly homogeneous with Fo_{70-72} (67%; group B), while 33% are slightly reversely zoned with Fo_{70-71} cores and Fo_{72-75} rims (subgroup A2) (Fig. 6a). Reaction rims are rare and limited to olivine crystals of subgroup A2; these are less developed compared to the 24 November 2009 olivine crystals. There is no correlation between MIs occurrence within the phenocrysts and MIs size. Olivine phenocrysts of 3 May 2009 are almost all homogeneous and show evolved compositions (Fo_{70-73}; group B), suggesting they were inherited from the HP magma (Fig. 6a).

For the 24 November 2009 major explosion, Fe–Mg diffusion timescales range from a few days to 4 weeks (Fig. 6b), with only one sample (STN8-02) indicating timescales on the order of hours. Overall, these timescales are shorter than those inferred for the 19 July 2020 major explosion (~20–25 days, max. of 2 months; Voloschina et al. 2023), for the July and August 2019 small-scale paroxysms (5–115 days; Métrich et al. 2021) and the 1456 and 1930 CE large-scale paroxysms (2–58 days; Métrich et al. 2021). Diffusion profiles of the 8 November 2009 major explosion indicate timescales significantly shorter than those associated to other major explosions, in the order of only hours to a maximum of 1.5 day.

Olivine spot compositions and diffusion profiles are reported in Table S4 (in Supplementary Material 1) and Table S7-S9 (in Supplementary Material 2), respectively, while timescale results are reported in Figs. 6b and S11 (Supplementary Figures) and in Table S10 (Supplementary Material 2).

Volatiles in melt inclusions

Melt inclusions from the 24 November 2009 olivine crystals have H_2O contents that range from 0.22 to 2.37 wt.% (Fig. 7). Within this variability, melt inclusions with lower

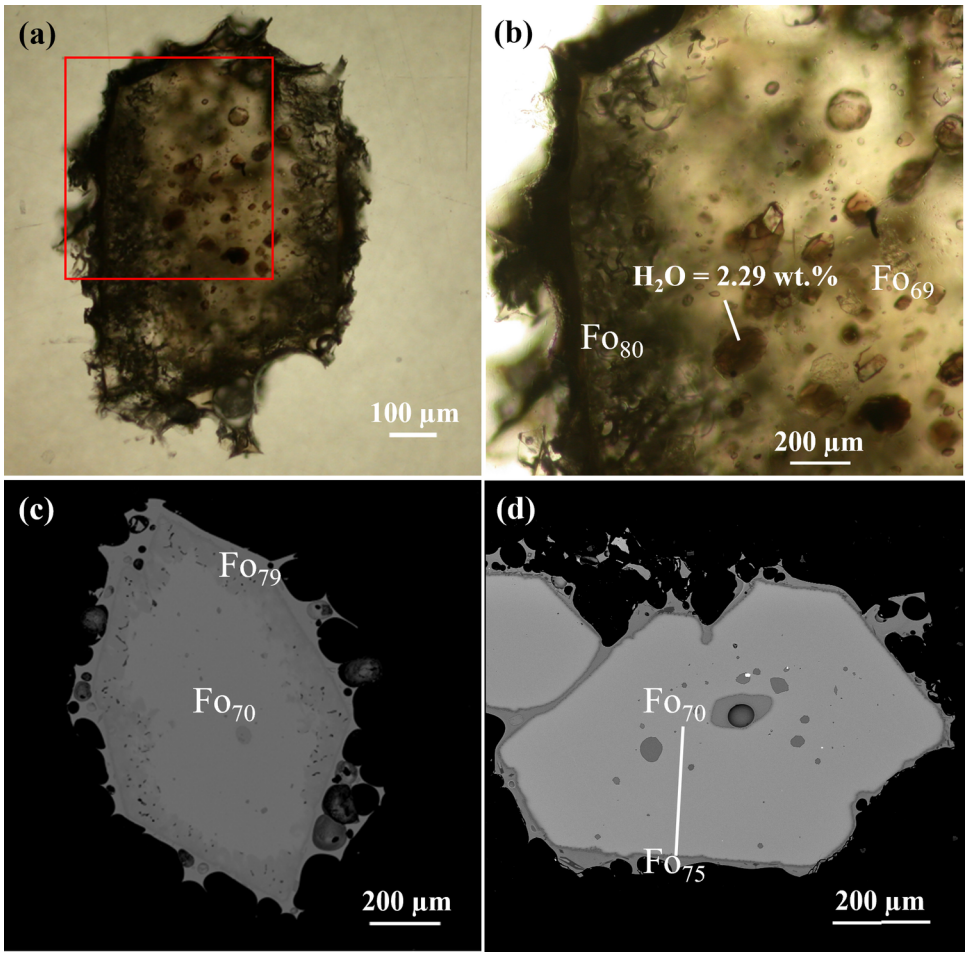

Fig. 5 **a** Transmitted light microphotograph of an evolved olivine phenocryst from the 24 November 2009 clasts. Red insert is in **b** where is shown a high-H_2O melt inclusion in intermediate position between the evolved Fo_{69} core and the more primitive Fo_{80} olivine rim. This is a case of post-entrapment rehydration of melt inclusion by the LP melt observed in several reversely zoned olivine phenocrysts from the 24 November 2009. **c** Olivine phenocryst from 24 November with thick Mg-richer reaction rim and evolved resorbed core. **d** Fe–Mg diffusion profile measured in an olivine phenocryst from the 8 November hosting several large melt inclusions in its core. Numbers refer to forsterite component in olivine (Fo% = 100 × Mg/(Mg + Fe))

H_2O contents (0.22–0.87 wt.%) are hosted by evolved and homogeneous or slightly reverse Fo_{70} olivine. Melt inclusions with higher H_2O contents (1.42–2.37 wt.%) are hosted mostly in evolved olivine crystals ($Fo_{69\text{-}71}$) that are strongly reversely zoned (up to Fo_{83}), and only in one case slightly reversely zoned (Table S2 in Supplementary Material 1). Some of these H_2O-rich MIs occupy an intermediate position between the evolved core and the more primitive rim (Fig. 5a, b). CO_2 is always below the detection limit (50 ppm), except for one larger (180 × 100 µm) and bubble-bearing melt inclusion — located close to the rim of a homogeneous Fo_{70} olivine — that contains 576 ppm of CO_2. Sulphur and chlorine are highly variable, ranging between 60 and 993 ppm (with a primary mode at 309 ppm) (Fig. 8) and 660–2990 ppm (primary mode at 1585 ppm), respectively. Embayments have lower and less variable H_2O contents, ranging from 0.31 to 0.57 wt.%, CO_2 below the detection limit, and sulphur and chlorine ranging between 216–220 ppm and 1320–1180 ppm (values on one melt embayment), respectively.

Melt inclusions of the 8 November 2009 samples have H_2O contents from 0.55 wt.% to below the detection limit, and CO_2 always below the detection limit. S contents range from 55 to 777 ppm, with a primary mode at 187 ppm. Chlorine contents range between 1050 and 2600 ppm, overlapping the 24 November 2009 melt inclusion range. Melt embayments have H_2O contents of 0.18–0.47 wt.%, comparable to melt inclusions, and CO_2 below the detection limit. Sulphur range between 168 ppm to below the detection limit and chlorine contents vary between 1150 and 1310 ppm.

Melt inclusions of 3 May 2009 have H_2O contents ranging from 0.15 to 0.75 wt.%, CO_2 always below the detection limit, S ranging from 619 ppm to below the detection limit and Cl of 772–2779 ppm.

Sulphur and chlorine contents in glassy groundmass wetting the olivine phenocrysts range between 31–285 ppm and 910–1405 ppm, respectively. These values are lower than those of melt inclusions and are comparable for the 24 November, 8 November and 3 May 2009 samples.

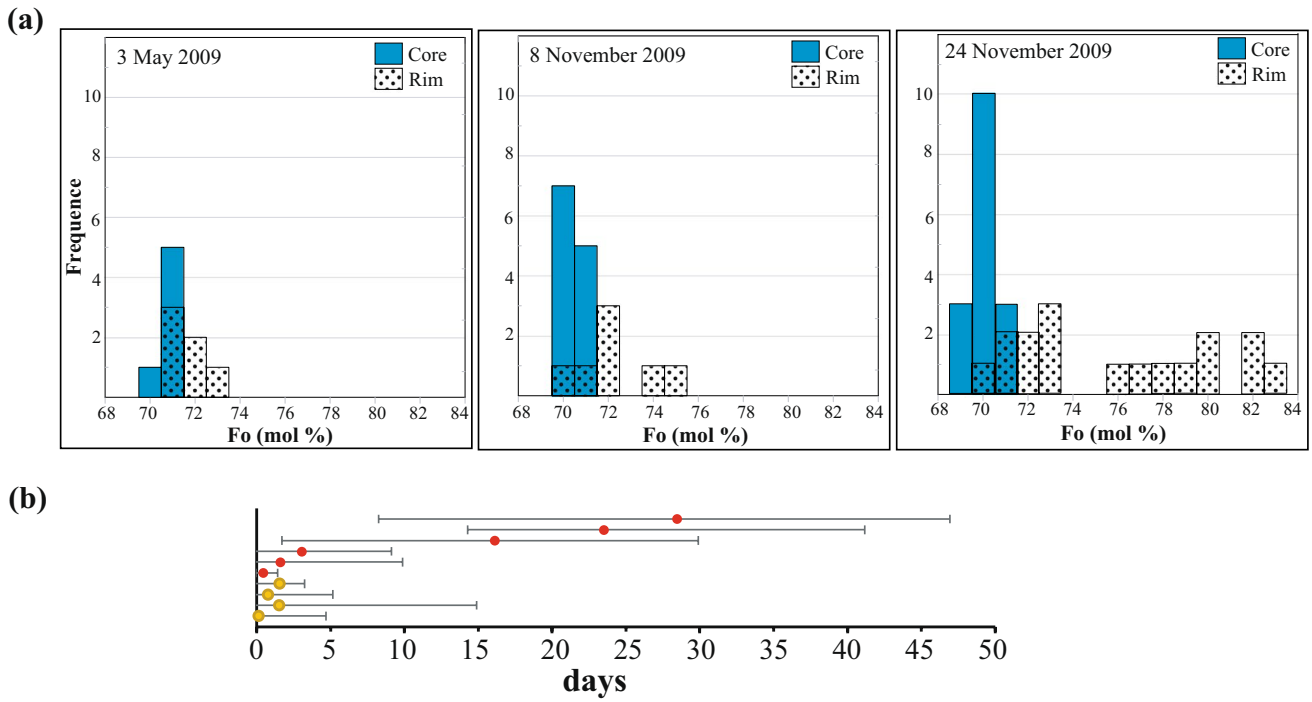

Fig. 6 **a** Histogram of olivine populations from the 24 November, 8 November and 3 May 2009 major explosions, comparing core and rim composition. **(b)** Diffusion timescales (in days) calculated in DIPRA (Girona and Costa 2013) in olivine phenocrysts from the 8 November (yellow filled dots) and 24 November (red filled dots) 2009 major explosions and associated uncertainty (based on the uncertainty in temperature and concentration) indicated with grey error bars

Volcanic gas composition and fluxes

The here presented melt inclusion results are complemented with previously published (Aiuppa et al. 2011) results for the composition/flux of the Stromboli volcanic gas plume. Results (Fig. 9) indicate that, throughout 2009, the SO_2 flux remained stable and low, with a mean average of 142 ± 59 (σ) tons/day. In contrast, the CO_2 flux was more variable and ranged between 65 and 7004 tons/day. The (molar) CO_2/SO_2 ratio varied between ~ 1 and 31.

Remarkable gas changes preceded the 24 November major explosion (Fig. 9). In particular, the explosion was associated with an abrupt increase of the CO_2/SO_2 ratio that started only a few hours before the explosive event. The CO_2 flux also abruptly increased to 2736 tons/day the day of the major explosion and peaked at 7004 tons/day the day after. The 3 May major explosion was also associated with some, less prominent gas changes. The median molar CO_2/SO_2 ratio in the volcanic plume (Fig. 9a) was ≤ 10 from January until late April, when it started to increase to > 15 molar ratio, remaining high until the 3 May 2009 major explosion. Few days before the 3 May major explosion, the CO_2 flux also increased, peaking at 1836 tons/day on 1 May. The 8 November explosion was not associated with any evident gas change, although it occurred during a phase of relatively high CO_2 fluxes.

Discussion

Pre-eruptive magma storage conditions

One critical question to address at Stromboli is whether (i) the shallow conduit system or (ii) the deep magma feeding system (or both) are involved in the generation of major explosions. Pre-eruptive volatile contents, as recorded by melt inclusions, can help to constrain the depth(s) of pre-eruptive magma storage (i.e., Anderson and Brown 1993; Métrich and Wallace 2008; Wallace et al. 2015b, 2021; Lerner et al. 2024).

Most melt inclusions of the 24 November 2009 display the typical composition of HP melt ($K_2O > 4$ wt.%; CaO/Al_2O_3 ~ 0.5), with S content as low as 0.1–0.2 wt.%, and CO_2 below the detection limit. Conversely, they display highly variable H_2O contents from 0.4 wt.% to 2.37 wt.% (Figs. S4, S5 in Supplementary Figures). Both relatively low H_2O (0.4 wt.%) and Al_2O_3 (~ 15 wt.%) concentrations are indicative of significant plagioclase crystallization typical of the crystal-rich magma residing in the upper parts of the volcano (Landi et al. 2004, 2022). Accordingly, these melt inclusions record a strongly degassed magma. Instead, relatively high H_2O content (> 1.5 wt.%,

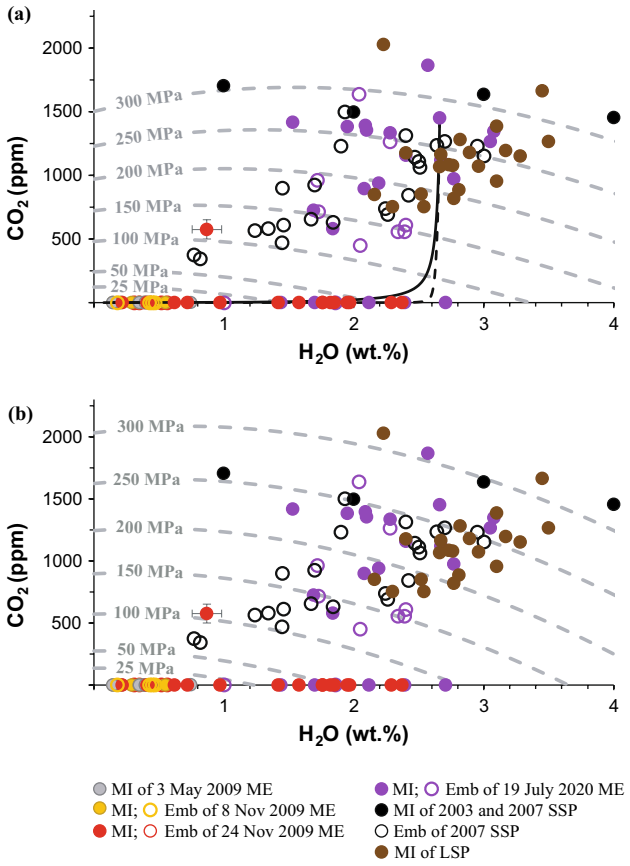

Fig. 7 Dissolved CO_2 and H_2O (wt.%) in melt inclusions (filled dots) and embayments (empty dots) from the 3 May, 8 November and 24 November 2009 major explosions (ME) in comparison with 19 July 2020 major explosion (Voloschina et al. 2023), 5 April 2003 and 15 March 2007 small-scale (SSP) paroxysms (Métrich et al. 2005, 2010) and historic large-scale (LSP) paroxysms (Bertagnini et al. 2003; Métrich et al. 2010). Isobars in MPa (grey dashed lines) were calculated in VESIcal (Iacovino et al. 2021) using an averaged melt composition from the 19 July 2020 major explosion (see Table S6, Supplementary Material 1) at 1150 °C. **a** Isobars and a general degassing path (solid line = open system; dashed line = closed system) of a 19 July 2020 melt inclusion were modelled using the MagmaSat solubility model (Ghiorso and Gualda 2015). **b** Isobars were modelled using the Iacono-Marziano solubility model (Iacono-Marziano et al. 2012). The maximum errors for H_2O and CO_2 (13%) determined in the 3 May, 8 November and 24 November 2009 melt inclusions and embayments are indicated as error bars

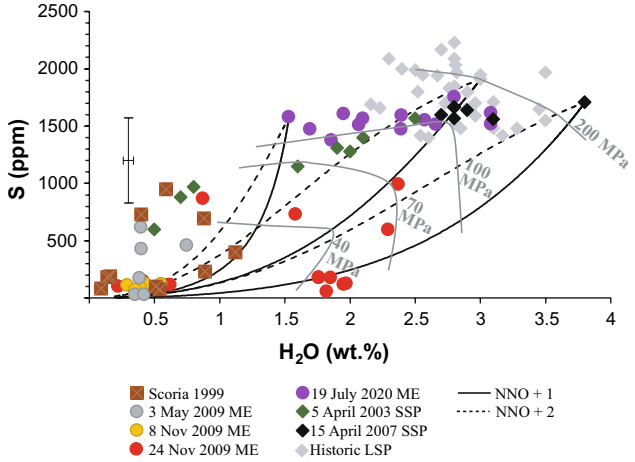

Fig. 8 Sulphur (ppm) vs H_2O (wt.%) contents in melt inclusions of the 3 May, 8 November and 24 November 2009 major explosions (ME; this study), in comparison with the 19 July 2020 major explosion (Voloschina et al. 2023), 5 April 2003 small-scale paroxysm (SSP; Métrich et al. 2005), 15 March 2007 small-scale paroxysm (SSP; Métrich et al. 2010) and historic large-scale paroxysms (LSP; Bertagnini et al. 2003; Métrich et al. 2010). Black lines show a general degassing path modelled by using the Iacono-Marziano model (Iacono-Marziano et al. 2012). Runs were performed at 1150 °C, assuming a fo_2 NNO + 1 (black solid line) and NNO + 2 (black dashed line). Grey lines indicate isobars in MPa. Average error relative to S = 31% and maximum error for H_2O = 13% are indicated as error bars

Fig. S5) is inconsistent with very low dissolved sulphur concentrations (Fig. 8), massive plagioclase crystallization (Di Carlo et al. 2006) and relatively low Al_2O_3 content which has been analysed (Table S2). The high-H_2O melt inclusions of the 24 November event are entrapped in strongly reversely-zoned olivine crystals from $Fo_{69\text{-}71}$ in the core to $Fo_{82\text{-}83}$ in the rims. These latter olivine compositions are in equilibrium with LP-type glassy groundmass ($CaO/Al_2O_3 \sim 0.60$, Fig. S3 in Supplementary Figures). As a whole, these observations strongly suggest H_2O (H^+) re-equilibration of the initially almost dry melt inclusions through the olivine ($Fo_{69\text{-}71}$) as experimentally reported for the olivine-hosted MIs of the Galapagos Plateau basalt (Portnyagin et al. 2008). In all melt inclusions, CO_2 is below the detection limit, which suggests extensive degassing took place before MI entrapment. A maximum CO_2 content of 576 ppm has been detected exclusively in an intermediate and bubble-bearing melt inclusion (sample STN8-15-M7). The measured value represents only the CO_2 content dissolved in the melt; however, CO_2 is known to be severely partitioned into shrinkage bubble (Hartley et al. 2014; Moore et al. 2015; Wallace et al. 2015a, b, 2021; Maclennan 2017; Robidoux et al. 2018; Tucker et al. 2019; Rasmussen et al. 2020; Wieser et al. 2021; Buso et al. 2022). As such, the measured CO_2 content likely underrepresents the total amount originally dissolved in the melt. This melt inclusion is located near the Fo_{70} olivine rim which is in equilibrium with the groundmass (HP), hence was not affected by post-entrapment processes of rehydration, consistent with its low H_2O content (0.87 wt.%).

We exclude from the P_{sat} calculations those melt inclusions that recorded high-H_2O content in the 24 November 2009 event, as they have been affected by secondary rehydration processes, and therefore their values do not represent pressure values at the time of the MI entrapment. Similarly,

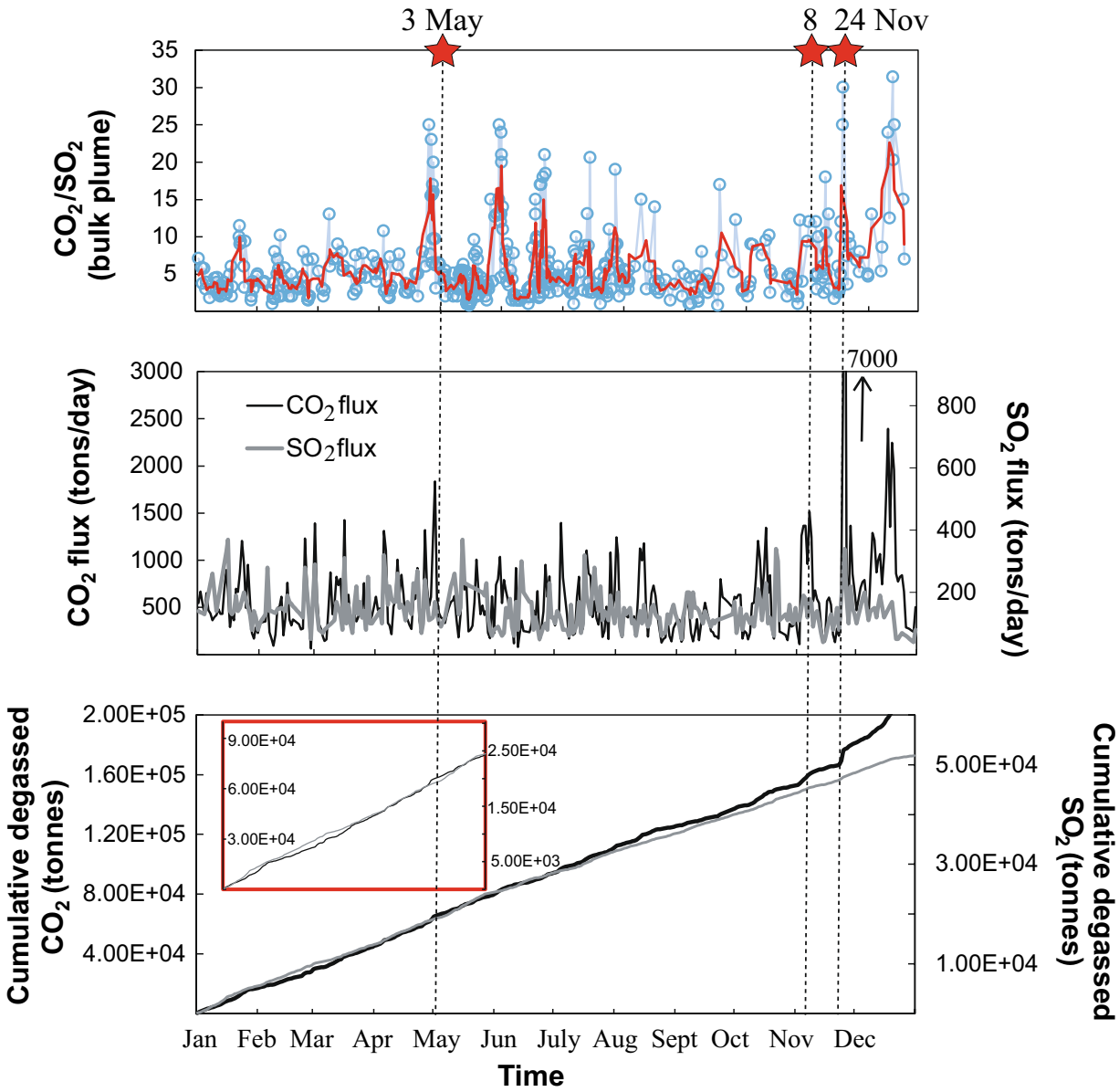

Fig. 9 Gas plume observation at Stromboli during the 2009 year. **a** CO_2/SO_2 ratio in the bulk plume. **b** CO_2 (black line) and SO_2 (grey line) fluxes (in tons/day). **c** Cumulative CO_2 (black line) and SO_2 (grey line) fluxes. The CO_2 scale is 3.3 times higher than the SO_2 scale in order to normalise it to the time-averaged CO_2/SO_2 ratio of Stromboli's emission during the observation period. The red line indicates the weekly mobile average, whereas the red stars indicate the onset of the 3 May, 8 and 24 November major explosions. The red insert shows a focus on the 3 May 2009 event: the CO_2 flux decelerated relative to the SO_2 flux in the months prior the onset of the eruption, followed by a convergence of the two cumulate CO_2 and SO_2 fluxes

based on the position close to the olivine's rim and intermediate-composition of STN8-15-M7, we cannot rule out that it recorded a late episode of magma mixing, thus its volatile composition was excluded from further calculation.

Here, our saturation pressure calculations are based on a comparison between two models, the MagmaSat solubility model (Ghiorso and Gualda 2015) and the Iacono-Marziano solubility model (Iacono-Marziano et al. 2012), both implemented in VESIcal (Iacovino et al. 2021). The former has been calibrated for a wide range of compositions, temperatures and pressures and has been used for the pressure calculations based on high H_2O and CO_2 contents in melt inclusions for the 19 July 2020 major explosion ($H_2O = 1.53–3.64$ wt.% and $CO_2 = 580–1866$ ppm; Voloschina et al. 2023) as well as the recalculation of MIs for the 2003 and 2007 paroxysms (Métrich et al. 2010). On the other hand, while the calibration range of the experiments that underlie the Iacono-Marziano solubility model is more limited, it is specifically calibrated on alkali-basaltic melt compositions (Iacono-Marziano et al. 2012). Most

importantly, the latter can be implemented in the Sulfur_X model of Ding et al. (2023), thus allowing to model sulphur degassing (see following sections).

The H_2O vs. CO_2 plot (Fig. 7a, b) shows the isobars modelled at 1150 °C using an averaged LP intermediate melt composition, in equilibrium with Fo_{80-83} olivine crystals, taken from the 19 July 2020 dataset (Voloschina et al. 2023; composition resumed in Table S6, Supplementary Material 1), comparing the isobars modelled using the MagmaSat (Fig. 7a) or the Iacono-Marziano solubility model (Fig. 7b). What clearly emerges from this comparison between the two plots (Fig. 7a, b) is that the differences arising from the use of these two different solubility models are minimum at low pressure values (2009 major explosions), while differences are higher at high pressure values (19 July 2020 and paroxysms), showing deviation on saturation pressures up to 30 MPa for the 19 July 2020 major explosion.

Consequently, for the low H_2O and CO_2 contents measured in melt inclusions of all the 2009 major explosions, both models yield similarly low entrapment pressures, lower than 10 MPa (Iacono-Marziano et al. 2012 solubility model) and lower than 7 MPa (MagmaSat solubility model). These pressures correspond to a shallow inferred depth, lower than 1 km below the sea level (b.s.l.) (assuming an average crustal density of 2700 kg/m^3).

To complement the above set of information, and in particular considering that saturation pressures for 2009 melt inclusions are based on H_2O contents only, we also attempt a degassing estimate based on the sulphur (S) vs. H_2O systematics (Fig. 8). We used Sulfur_X v1.1 (Ding et al. 2023) to model the S degassing behaviour (in combination with H_2O and CO_2) during magma ascent and decompression (down to 1 atm) under closed-system conditions. This code combines a calibration of experimentally derived sulphur partition coefficients between silicate melt and co-existing vapor phase with an existing C-O-H solubility model (in this case, the Iacono-Marziano solubility model). However, large uncertainties arise for sulphur partition coefficients at < 25 MPa, as no experimental sulphur partition coefficients exist at such low-pressure conditions.

Three couples of independent model degassing paths were generated, all at 1150 °C and fO_2 ranging from NNO + 1 (black solid line) to more oxidised (NNO + 2; black dashed line) conditions. Each of the three couples were obtained by initialising the model runs for a given set of starting melt compositions (composition reported in Table S6, Supplementary Material 1), and exemplified by MIs of the: (i) 19 July 2020 major explosion (H_2O = 1.5 wt.% and S = 1582 ppm; Voloschina et al. 2023); (ii) 15 March 2007 small-scale paroxysm (H_2O = 3.8 wt.% and S = 1710 ppm; Métrich et al. 2010) and (iii) a historic large-scale paroxysm (H_2O = 3 wt.% and S = 1910 ppm; Métrich et al. 2010) with high S and H_2O contents.

Results of model simulations of degassing are compared against MIs information in Fig. 8. Model simulations indicate sulphur begins to exsolve at rather high pressures, consistent with experimental data on Stromboli oxidised melts (Lesne et al. 2011) and previous melt inclusions study (Métrich et al. 2021), indicating S degassing from as deep as at 150 MPa (~ 5 km b.s.l.). Below this pressure, model lines reasonably reproduce the coupled drop of S and H_2O concentrations recorded in MIs of the 2009 major explosions (this study), and also of glass embayments of the 2020 major explosion and of the 2003 paroxysms. This comparison therefore suggests shallow entrapment pressures for the 2009 melt inclusions, that are consistent with those previously calculated from H_2O contents only (entrapment pressures of < 10 MPa; Fig. 7). By contrast, in the high-pressure range (150–200 MPa), MIs from the 19 July 2020 major explosion and from the small- and large-scale historic paroxysms exhibit an overall tendency of decreasing H_2O at constant S, interpreted to represent isobaric magma dehydration caused by flushing by CO_2-rich bubbles (Métrich et al. 2010; Voloschina et al. 2023).

In summary, the inferred MIs entrapment depths indicate that the 2009 major explosions predominantly drained material originally stored in the upper feeding conduit system, at source depths lower than 400 m b.s.l., corresponding to the shallower portion of the dyke-conduit feeding system, which extends from surface to ~ 1–2 km b.s.l. depth (Chouet et al. 2003, 2008; Patanè et al. 2017).

Pre-eruptive processes and mixing to eruption timescales

During the last two decades, extensive scientific research has corroborated the idea for the existence of a vertically extended plumbing system at Stromboli, in which a complex interplay of fractional crystallization, crystal dissolution, magma mixing and degassing concur to control magma evolution (Bertagnini et al. 2003; Francalanci et al. 1988, 1989, 2004; Landi et al. 2004, 2008, 2022; Métrich et al. 2001, 2010, 2021). By integrating compositional results for host olivine crystals, melt inclusions and glassy groundmass, we here attempt to refine our understanding of the driving pre-eruptive processes of the intermediate, yet highly hazardous category of explosive events represented by the major explosions.

One key observation is that olivine crystals in all the 2009 products are relatively low in Mg, with evolved (Fo_{69-72}) olivine cores, and relatively flat Fe–Mg compositional profiles over hundreds of micrometres (Fig. S11 in Supplementary Figures). This, combined with the dominant HP compositional affinity of the melt inclusions (Figs. 3, 4), and their low volatile contents, suggest these minerals formed during protracted magma storage in a shallow reservoir. If then

major explosions are triggered by overpressure development in the shallow HP magma reservoir, the question that arises is what drives this overpressure, and over what timescales.

The rapid ascent of deeply-stored LP magma, and its mingling with the shallow HP magma, has long been invoked as a key driver of the larger than normal explosions at Stromboli (Bertagnini et al. 2003; Di Carlo et al. 2006; Métrich et al. 2001, 2010, 2021; Pichavant et al. 2009, 2022). The recurrent reverse zoning (Fig. 6) observed in olivine phenocrysts from the 24 November major explosion (with rims up to Fo_{83}) and (to a minor extent) from the 8 November major explosion, supports pre-eruptive interaction between shallow-stored HP phenocrysts and Mg-richer melts. Two additional lines of evidence corroborate this process. First, for both eruptions, the glassy groundmass is compositionally more primitive than the olivine-hosted MIs, partly overlapping the LP compositional field (Figs. 3, 4). Secondly, the 24 November olivine phenocrysts contain abundant (and pervasive) resorption textures (Fig. 5a–c, Fig. S1 in Supplementary Figures; these are also present — although less commonly — in the 8 November olivine crystals). These resorption textures implicate that, following a long-lived period of equilibrium crystallization within the shallow resident magma (during which cores with evolved composition ~ Fo_{70} were formed), higher-temperature and water-richer melts rapidly entrained the system, causing the redissolution of the phenocryst rims (Streck 2008). Taken together, these lines of evidence suggest a trigger mechanism for major explosions in which deeply rising, volatile-rich LP magma is rapidly injected into the shallow HP magma storage zone (see also Voloschina et al. 2023). The presence of resorbed olivine crystals is fully consistent with the reactivation — during the more energetic major explosions (particularly the 24 November event) — of the stagnant crystal-mush zone by the influx of the deep LP magma (Bertagnini et al. 2003; Di Stefano et al. 2020; Francalanci et al. 2004, 2005, 2012; Métrich et al. 2021; Petrone et al. 2022).

The timescales of this pre-eruptive HP-LP interaction can be inferred from modelling of diffusion profiles in olivine rims (e.g., Costa et al. 2020) (Fig. 6b). Overall, olivine cores of the November major explosions suggest a protracted storage in the shallow reservoir, whereby olivine crystals completely equilibrate through diffusion in steady-state conditions. In particular, olivine crystals of the 8 November explosion document short mixing to eruption timescales, in the order of hours to < 2 days. These temporal timescales are shorter than those required for extensive mixing between HP and LP magmas — as, at least in principle, required to explain the intermediate compositions observed in the glassy groundmasses from the 8 November eruption (La Felice and Landi 2011; Landi et al. 2022). We hence propose rapid HP-LP interaction was favoured (Perugini et al. 2003; De Campos et al. 2011) by vigorous ascent of deeply-rising gas bubbles, as suggested by gas data (see below).

A wider range of timescales, from hours to a maximum of 4 weeks, is recorded by olivine crystals of the 24 November explosions. The 4 weeks upper limit is longer than the eruptive inter-event time (the 16 days elapsed between the 8 and 24 November explosions). We argue that degassed and dense (unerupted) HP magma, left from the previous eruptive activity in the shallow reservoir, was re-mobilised by the ascending bubbly LP magma in the eruption run-up.

In contrast to the November events, the investigated 3 May 2009 products show no evidence of more primitive (LP magma-like) glassy groundmass (Figs. 3–4; note that some rare, more primitive groundmass has been however reported for this eruption; Corsaro and Miraglia 2009a; La Felice and Landi 2011; Pioli et al. 2014, who analysed the distal fraction of the tephra deposit made by a few scattered lapilli). This absence/rarity of LP magma-like groundmass is consistent with the smaller LP erupted mass in the 3 May eruption ($1.8–2.9\times10^4$ m^3, relative to $4.4–6.5\times10^5$ m^3 for the 24 November eruption; Pioli et al. 2014). The 3 May major explosion olivine crystals are also compositionally homogeneous (only one olivine exhibits some slight reverse zoning). In summary, these results suggest that the LP magma was only marginally involved in the triggering of the 3 May major explosion, requiring a distinct mechanism.

Clues from volcanic gas plume monitoring

Volcanic gas observations corroborate a distinct trigger mechanism for the May and November 2009 major explosions. We rely here on the gas dataset already presented and discussed in Aiuppa et al. (2011) (Fig. 9a, b). These data are used to calculate the cumulative masses (in tonnes) of degassed CO_2 and SO_2 throughout 2009, illustrated in Fig. 9c (note that the CO_2 scale is 3.3 times higher than the SO_2 scale in order to match the time-averaged CO_2/SO_2 mass ratio). This diagram highlights a contrasting degassing behaviour for the periods preceding the November and May 2009 explosions, respectively.

In the months prior to the November explosions, the CO_2 flux accelerated relative to the SO_2 flux, as indicated by the diverging cumulative trends (Fig. 9c). This CO_2 acceleration started sometime in late summer 2009, and became more pronounced in mid- to late-October, e.g., weeks to days prior to the first major explosion on November 8 (Fig. 9c). The peak of CO_2 flux was observed in correspondence of the 24 November explosion (see Fig. 9b). Taken together, and considering the CO_2-rich nature of Stromboli's deep LP magma (relative to the HP magma that is CO_2-depleted), these data are consistent with a mechanism in which the November explosions were preceded by an anomalous inflow of CO_2-rich gas bubbles, transported by (with) the ascending LP

magma (as testified by olivine zoning and groundmass chemistry; see the "Pre-eruptive processes and mixing to eruption timescales" section). A similar mechanism was proposed for the July 2020 major explosion (Voloschina et al. 2023) and is hence likely to be a common characteristic of the more energetic events (those erupting larger LP pumice volumes).

No obvious CO_2 acceleration was observed prior to the 3 May 2009 event. In contrast, in the months prior the 3 May major explosion, the CO_2 flux decelerated relative to the SO_2 flux (from February to mid-March, see inset in Fig. 9c), followed by a recovery phase during which the two cumulate flux trends converged again (e.g., the CO_2/SO_2 mass ratio returned to its time-averaged value). The peak CO_2 was observed in the days prior to the 3 May blast. Aiuppa et al. (2011) explained these cycles of decelerating/accelerating CO_2 to be caused by (i) an initial phase of gas bubbles retention at depth (causing a deceleration of the CO_2 flux), gradually accumulating a foam at some (rheological or structural) discontinuity (Allard 2010; Aiuppa et al. 2011; Caricchi et al. 2024), followed by (ii) a precursory phase of passive gas leakage from the growing foam (CO_2 flux acceleration; Phillips and Woods 2001), and subsequent (iii)

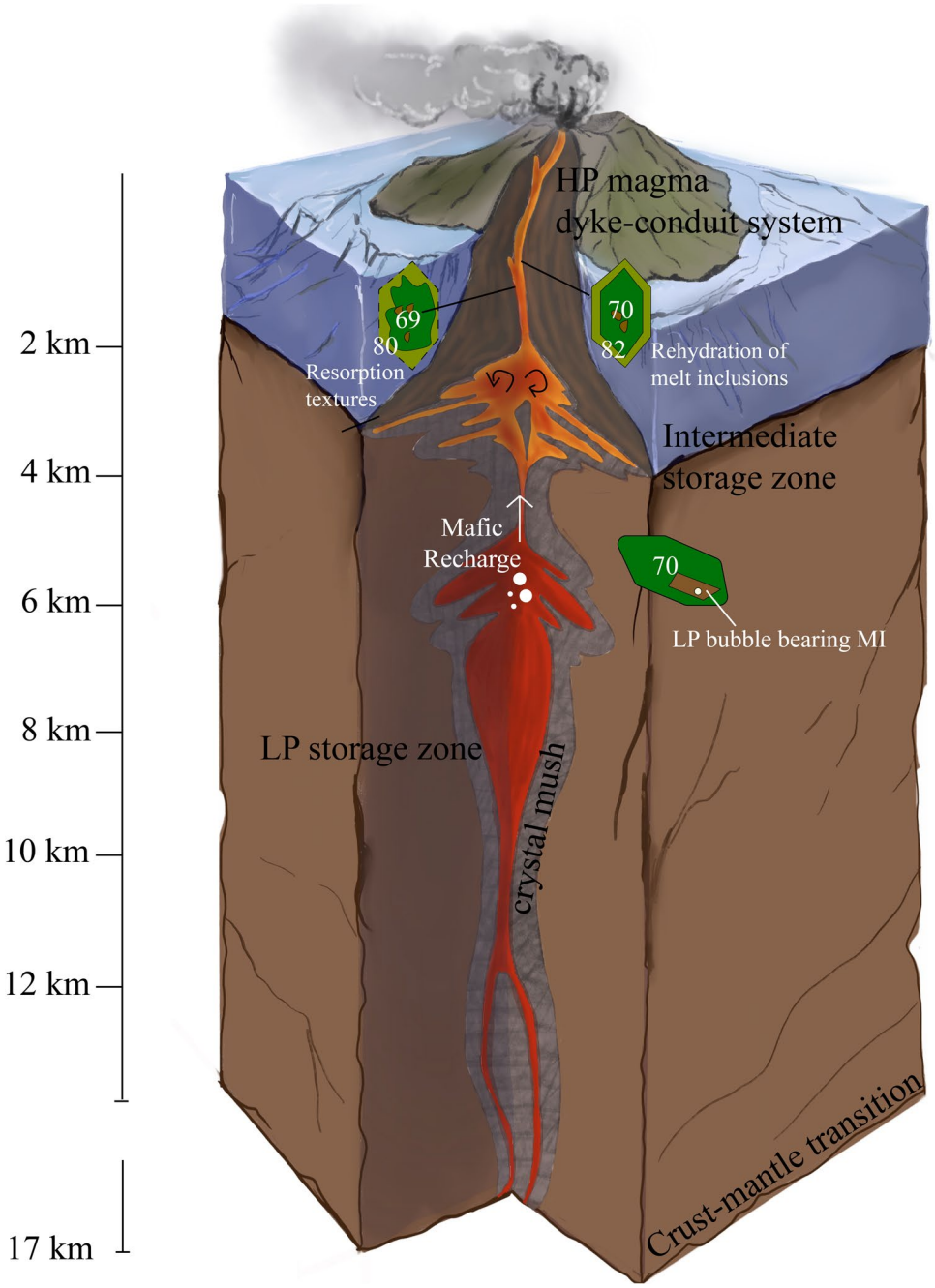

Fig. 10 Interpretative model of Stromboli's plumbing system explaining the pre-eruptive dynamics of the 24 November 2009 major explosion, based on (i) major element and sulphur contents on melt inclusions, embayments, glassy groundmass and host olivine crystals, (ii) dissolved H_2O and CO_2 contents on melt inclusions and embayments, and (iii) olivine textures

catastrophic collapse of the foam, leading to the fast ascent and surface bursting of gas slugs during the major explosion (Allard 2010). This mechanism does not require any important pre-event upward migration of LP magma, which would be difficult to reconcile with our mineral and glass chemistry results (see above).

In summary, gas and petrological results (host olivine composition, MIs and glassy groundmass compositions) indicate there may be no single mechanism to explain the generation of major explosions. Rather, these events can either be gas-driven (e.g., caused by gas accumulation and then failure of a foam) or magma-driven (e.g., caused by the upward migration of small pockets of deep volatile-rich magma, causing pressure build-up in the shallow HP reservoir). In this interpretation, key factors in modulating the diversity of explosion magnitude are (i) the relative proportions of gas and LP magma involved in the process, and (ii) the depth at which the gas bubble retention event (in the gas-driven scenario), or the LP-HP interaction event (in the LP magma-driven scenario) occur (Allard 2010; Métrich et al. 2021; Landi et al. 2022). We conclude that the low-intensity, 3 May 2009 major explosion was critically driven by the gas accumulation within the shallower (< 1 km b.s.l.) magma reservoir, implicating a marginal involvement of the deep LP plumbing system. In contrast, a more active role for the deep LP magma is implicated for both November 2009 events. In this case, the rising LP magma interacted (over timescales of days to weeks) with the shallow HP magma reservoir and with the surrounding crystal mush zone, ultimately causing a more deeply-sourced, and hence more energetic, series of explosions (Andronico and Pistolesi 2010) (Fig. 10).

Linking ground deformation patterns to eruptive intensity

Following our discussions of volcanic gas and petrological insights, we now focus on the analysis of the ground deformation measured during the 2009 major explosions.

In Fig. 11a, the ground deformation (tilt) filtered for the Very-Long Period (VLP) seismic signal is reported. The 3 May 2009 produced a ground tilt of ~ 0.2 µrad recorded by tiltmeters, while the 8 and 24 November events produced a ground tilt of 0.48 and 0.32 µrad, respectively. The measurements of the ground deformations confirm the 3 May 2009 as the lowest-intensity major explosion among the studied 2009 events, but also raise the question as to how the 8 November major explosion produced a higher ground deformation, despite having ejected smaller magma volumes and having smaller dispersal areas (10,000 m^2) than the 24 November event (15,000 m^2; Andronico and Pistolesi 2010). To explain this apparent discrepancy in the deformation amplitude, we highlight the 24 November is the result of two different blasts occurring ~ 15 s apart which contributed to a slightly larger total volume. In the whole, the amplitude

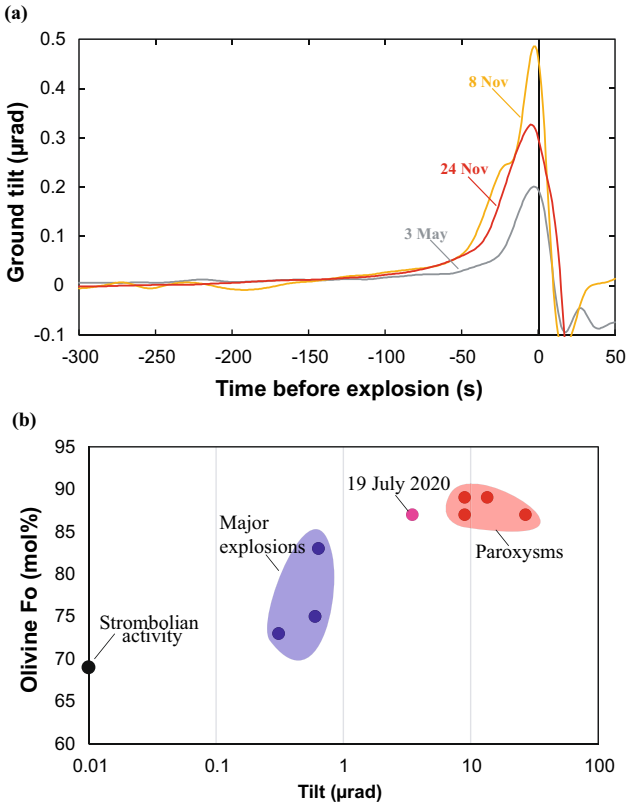

Fig. 11 **a** Ground deformation (tilt), filtered for the Very-Long Period signals, associated with the 2009 major explosions. Note that the chosen time frame (X axis) is consistent with the observation that the ground inflation becomes more visible ~ 300 s before the onset of each major explosion. **b** Semilog plot of tilt (µrad; contaminated with VLP) against olivine composition (Fo mol%) of regular Strombolian explosions to major explosions (3 May, 8 November and 24 November 2009, 19 July 2020) and paroxysms at Stromboli (5 April 2003; 15 March 2007; 3 July and 28 August 2019)

of the pre-explosion deformation falls within the range typical of major explosions class and scales with the magnitude/intensity of each explosion, depending on the volumes of the ejected material, as previously found by Ripepe et al. (2021).

Lastly, if we correlate the ground deformation measured by tiltmeters during the Stromboli's eruptive activity, spanning from its regular Strombolian explosions to paroxysms, to their respective olivine (forsterite) compositions (Fig. 11b), it becomes evident that the ordinary activity is associated to low ground deformation (0.1 µrad) and evolved Fo_{70} olivine, while major explosions range instead from 0.31 to 0.64 µrad with olivine composition from Fo_{73} to Fo_{83}. An exception to this is the 19 July 2020 event (3.5 µrad; Fo_{87} olivine), which falls between the 2009 events and the paroxysmal activity (9–27 µrad; $Fo_{87\text{-}89}$ olivine). What clearly emerges is also that, in agreement with the previous findings of Métrich et al. (2021) and Voloschina et al. (2023), the olivine chemistry display a good correlation with the tilt measurements, thus with the eruption intensity/magnitude of the explosions.

Conclusions

Stromboli exhibits eruptions ranging in size from regular Strombolian explosions to paroxysms, whose diversity is governed by the (variable) interplay between the shallow HP magma and gas ± magma supply from depth (Pioli et al. 2014; Métrich et al. 2021; Voloschina et al. 2023). The regular Strombolian-type explosions are sustained by the shallow-stored HP magma (with rare LP clasts interpreted as fragments dragged to the surface by deep CO_2-rich gas bubbles; D'Oriano et al. 2011). In contrast, the roles of deeply sourced bubbles and LP magma increase with increasing eruption magnitude/intensity. For example, the smallest major explosions (at the upper boundary of regular Strombolian-type explosions) do not emit LP products (i.e., 8 September 1998, Bertagnini et al. 1999; 7 September 2008; Calvari et al. 2012), or they do in negligible amounts (3 May 2009, Corsaro and Miraglia 2009a; La Felice and Landi 2011; Pioli et al. 2014). In contrast, higher volumes of LP magma are emitted during the most violent major explosions (8 and 24 November 2009, Corsaro and Miraglia 2009b,c; Pioli et al. 2014; La Felice and Landi 2011; Landi et al. 2022; this study; 19 July 2020, Voloschina et al. 2023) and small to large-scale paroxysms (5 April 2003, 15 March 2007 and historic events, Bertagnini et al. 2003; Métrich et al. 2005, 2010), implicating the involvement of the deep plumbing system.

The results presented here indicate that the diversity in style and magnitude observed within the eruptive class of major explosions likely reflects distinct eruption triggering mechanisms. We have shown that the November explosions contain mineralogical, textural and petrological evidence for the injection of variable volumes of LP magma within the HP magma reservoir. This process is likely to have taken place over timescales of hours (8 November) to weeks (24 November), and to have caused overpressure development at the HP magma reservoir. In contrast, the 3 May products contain only homogeneous (un-zoned) olivine crystals with composition comparable to that of ordinary activity (~ Fo_{70}). The lack of resorption textures and low volatiles in MIs, coupled with the small amount of LP glassy groundmass (Corsaro and Miraglia 2009a; La Felice and Landi 2011; Pioli et al. 2014), confirm that the LP magma ascent played only a marginal role. Rather, in combination with volcanic gas plume results, our results indicate the 3 May eruption may have been triggered by a pressurization of the shallow (< 1 km b.s.l.) HP magma reservoir, caused by the accumulation of gas bubbles at some (rheological of structural) discontinuity. These diverse causal mechanisms, combined with short incubation timescales (hours to weeks), may explain why major explosions have remained so difficult to forecast (Aiuppa et al. 2025).

Supplementary Information The online version contains supplementary material available at https://doi.org/10.1007/s00445-025-01862-9.

Acknowledgements The authors are grateful to Yves Moussalam for careful editorial handling and useful comments and two anonymous reviewers for their thorough and insightful reviews. The authors thank Eleonora Braschi and Andrea Orlando from the joint laboratory (LaMA) of the DST and CNR-IGG of Firenze, and Andrea Risplendente from the University of Milan for their assistance with microprobe analyses, Patrizia Landi for providing the microprobe analysis data on the LP groundmass of the 3 May 2009, and Valeria Saieva for the artistic contribution to the realization of the interpretative model of Stromboli's plumbing system (Fig. 10).

Author contribution Laura Insinga: writing — original draft preparation, writing — review and editing, methodology, formal analysis and investigation, data curation, visualization, conceptualization. Marija Voloschina: writing — review and editing, methodology, formal analysis and investigation, data curation, visualization, conceptualization. Paola Marianelli: writing — review and editing, methodology, formal analysis, investigation, data curation, visualization, validation, conceptualization. Erika Bartolomeo: formal analysis and investigation, data curation. Antonella Bertagnini: writing — review and editing, validation, conceptualization. Nicole Métrich: writing — review and editing, validation, conceptualization. Silvio G. Rotolo: writing — review and editing, methodology, investigation, data curation, visualization, validation, conceptualization, project administration, supervision. Alessandro Aiuppa: writing — review and editing, resources, methodology, formal analysis and investigation, data curation, visualization, validation, conceptualization, funding acquisition, project administration, supervision. Maurizio Ripepe: methodology, formal analysis and investigation, data curation, conceptualization. Marco Pistolesi: writing — review and editing, resources, methodology, investigation, data curation, visualization, conceptualization, project administration, supervision.

Funding Open access funding provided by Università degli Studi di Palermo within the CRUI-CARE Agreement. This study received funding from the service activity enhancement project "Sviluppo del Sistema unico (INGV-Università) di monitoraggio vulcanico e rilevamento precoce dei maremoti e delle esplosioni parossistiche di Stromboli" funded by the Dipartimento della Protezione Civile and the INGV. The study/service/product does not necessarily reflect the policy and position of the Istituto Nazionale di Geofisica e Vulcanologia and Dipartimento della Protezione Civile, Italy. Funding was also made available by the RETURN Extended Partnership funded by the European Union Next-GenerationEU (National Recovery and Resilience Plan – NRRP, Mission 4, Component 2, Investment 1.3 – D.D. 1243 2/8/2022, PE0000005).

Data availability All the data discussed in the manuscript are presented in the figures and in the supplementary material.

Declarations

Conflict of interests The authors declare no competing interests.

References

Aiuppa A, Burton M, Allard P, Caltabiano T, Giudice G, Gurrieri S, Liuzzo M, Salerno G (2011) First observational evidence for the CO_2-driven origin of Stromboli's major explosions. Solid Earth 2:135–142. https://doi.org/10.5194/se-2-135-2011

Aiuppa A, Bitetto M, Delle Donne D, La Monica FP, Tamburello G, Coppola D, Della Schiava M, Innocenti L, Lacanna G, Laiolo M, Massimetti F, Pistolesi M, Silengo MC, Ripepe M (2021) Volcanic CO_2 tracks the incubation period of basaltic paroxysms. Sci Adv. https://doi.org/10.1126/sciadv.abh0191

Aiuppa A, Bitetto M, Curcio L, Donne DD, Lages J, Trisciuzzi GLB, Tamburello G, Vitale A, Cannavò F, Coltelli M, Coppola D, Innocenti L, Insinga L, Lacanna G, Laiolo M, Massimetti F, Pistolesi M, Privitera E, Ripepe M, Voloschina M, Cilluffo G (2025) Volcanic gas changes prior to Stromboli's major explosions are statistically significant. J Volcanol Geotherm Res. https://doi.org/10.1016/j.jvolgeores.2025.108325

Aiuppa A, Bertagnini A, Métrich N, Moretti R, Di Muro A, Liuzzo M, Tamburello G (2010) A model of degassing for Stromboli volcano. Earth Planet Sci Lett 295(1–2):95–204. https://doi.org/10.1016/j.epsl.2010.03.040

Allard P (2010) A CO_2-rich gas trigger of explosive paroxysms at Stromboli basaltic volcano, Italy. J Volcanol Geotherm Res 189:363–374. https://doi.org/10.1016/j.jvolgeores.2009.11.018

Anderson AT, Brown GG (1993) CO_2 contents and formation pressures of some Kilauean melt inclusions. Am Mineral 78:794–803

Andronico D (2009) Il parossismo eruttivo di Stromboli del 3 maggio 2009: osservazioni di campagna svolte nei giorni successivi. Internal report no. UFVG2009/20, INGV, Sezione di Catania, Italy. http://sowebapp.ct.ingv.it/oldweb/Report/RPTVSTRCEN20090503.pdf

Andronico D, Pistolesi M (2010) The november 2009 paroxysmal explosions at Stromboli. J Volcanol Geotherm Res 196:120–125. https://doi.org/10.1016/j.jvolgeores.2010.06.005

Andronico D, Corsaro RA, Cristaldi A, Polacci M (2008) Characterizing high energy explosive eruptions at Stromboli volcano using multidisciplinary data: an example from the 9 January 2005 explosion. J Volcanol Geotherm Res 176:541–550. https://doi.org/10.1016/j.jvolgeores.2008.05.011

Andronico D, Del Bello E, D'Oriano C, Landi P, Pardini F, Scarlato P, Vitturi MDM, Taddeucci J, Cristaldi A, Ciancitto F, Pennacchia F, Ricci T, Valentini F (2021) Uncovering the eruptive patterns of the 2019 double paroxysm eruption crisis of Stromboli volcano. Nat Commun 12:4213. https://doi.org/10.1038/s41467-021-24420-1

Von Aulock FW, Kennedy BM, Schipper CI, Castro JM, Martin DE, Oze C, Watkins JM, Wallace PJ, Puskar L, Bégué F, Nichols ARL, Tuffen H (2014) Advances in Fourier transform infrared spectroscopy of natural glasses: from sample preparation to data analysis. Lithos 206:52–64. https://doi.org/10.1016/j.lithos.2014.07.017

Barberi F, Rosi M, Sodi A (1993) Volcanic hazard assessment at Stromboli based on review of historical data. Acta Vulcanol 3:173–187

Barth A, Portnyagin M, Mironov N, Holtz F, Moussallam Y, Rose-Koga EF, Rasmussen D, Towbin H, Gonnermann H, Mutch EJF, Rotolo SG, Plank T (2024) Fast, furious, and gassy: Etna's explosive eruption from the mantle. Earth Planet Sci Lett 643:118864. https://doi.org/10.1016/j.epsl.2024.118864

Bertagnini A, Coltelli M, Landi P, Pompilio M, Rosi M (1999) Violent explosions yield new insights into dynamics of Stromboli volcano. Eos Trans Am Geophys Union 80:633–636. https://doi.org/10.1029/99EO00415

Bertagnini A, Métrich N, Landi P, Rosi M (2003) Stromboli volcano (Aeolian Archipelago, Italy): an open window on the deep-feeding system of a steady state basaltic volcano. J Geophys Res Solid Earth. https://doi.org/10.1029/2002JB002146

Bertagnini A, Di Roberto A, Pompilio M (2011) Paroxysmal activity at Stromboli: lessons from the past. Bull Volcanol 73:1229–1243. https://doi.org/10.1007/s00445-011-0470-3

Bertagnini A, Métrich N, Francalanci L, Landi P, Tommasini S, Conticelli S (2008) Volcanology and magma geochemistry of the present day activity: constraints on the feeding system. In The Stromboli Volcano: an integrated study of the 2002–2003 eruption. Am Geophys Union, pp 19–38. https://doi.org/10.1029/182GM04

Bevilacqua A, Bertagnini A, Pompilio M, Landi P, Del Carlo P, Di Roberto A, Aspinall W, Neri A (2020) Major explosions and paroxysms at Stromboli (Italy): a new historical catalog and temporal models of occurrence with uncertainty quantification. Sci Rep 10:1–18. https://doi.org/10.1038/s41598-020-74301-8

Burton M, Allard P, Muré F, La Spina A (2007) Magmatic gas composition reveals the source depth of slug-driven Strombolian explosive activity. Science 317:227–230. https://doi.org/10.1126/science.1141900

Buso R, Laporte D, Schiavi F, Cluzel N, Fonquernie C (2022) High-pressure homogenization of olivine-hosted CO_2-rich melt inclusions in a piston cylinder: insight into the volatile content of primary mantle melts. Eur J Mineral 34:325–349. https://doi.org/10.5194/ejm-34-325-2022

Calvari S, Buettner R, Cristaldi A, Dellino P, Giudicepietro F, Orazi M, Boschi E (2012) The 7 September 2008 Vulcanian explosion at Stromboli volcano: multiparametric characterization of the event and quantification of the ejecta. J of Geophys Res: Solid Earth 117. https://doi.org/10.1029/2011JB009048

Caricchi L, Montagna C, Aiuppa A, Lages JPN, Tamburello G, Papale P (2024) CO_2 flushing triggers paroxysmal eruptions at open conduit basaltic volcanoes. J Geophys Res Solid Earth. https://doi.org/10.1029/2023JB028486

Carn SA, Clarisse L, Prata AJ (2016) Multi-decadal satellite measurements of global volcanic degassing. J Volcanol Geotherm Res 311:99–134. https://doi.org/10.1016/j.jvolgeores.2016.01.002

Chouet B, Dawson P, Ohminato T, Martini M, Saccorotti G, Giudicepietro F, De Luca G, Milana G, Scarpa R (2003) Source mechanisms of explosions at Stromboli Volcano, Italy, determined from moment-tensor inversions of very-long-period data. J Geophys Res Solid Earth 108(B1):7. https://doi.org/10.1029/2002JB001919

Chouet B, Dawson P, Martini M (2008) Shallow-conduit dynamics at Stromboli Volcano, Italy, imaged from waveform inversions. Geol Soc Lond Spec Publ 307:57–84. https://doi.org/10.1144/SP307.5

Corsaro RA, Miraglia L (2009a) Composizione dei vetri dei prodotti eruttati durante l'evento esplosivo parossistico avvenuto a Stromboli il 3 maggio 2009. Internal report no. UFVG2009/22, INGV, Sezione di Catania, Italy. https://www2.ct.ingv.it/en/avvisi-e-bandi/doc_view/205-rptvgptr20090513.html. Accessed 21 Aug 2024

Corsaro RA, Miraglia L (2009b). Composizione dei vetri dei prodotti eruttati la sequenza esplosiva avvenuta a Stromboli giorno 8 novembre 2009. Internal report no. UFVG2009/84, INGV, Sezione di Catania, Italy. https://www2.ct.ingv.it/it/avvisi-e-bandi/doc_view/1175-composizione-dei-vetri-dei-prodo

tti-emessi-l-8-novembre-a-stromboli.html. Accessed 21 Aug 2024

Corsaro RA, Miraglia L (2009c) Composizione dei vetri dei prodotti eruttati durante la sequenza esplosiva avvenuta a Stromboli giorno 24 novembre 2009. Internal report no. UFVG2010/02, INGV, Sezione di Catania, Italy. https://www2.ct.ingv.it/en/rapporti/sismologia/doc_view/1380-composizione-dei-vetri-dei-prodotti-dell-esplosione-a-stromboli-del-24-11-09.html. Accessed 21 Aug 2024

Cristaldi A (2009a) Rapporto sull'evento esplosivo dello Stromboli del giorno 03/05/2009 ripreso dalle telecamere di sorveglianza. Internal report no. UFVG2009/018, INGV, Sezione di Catania, Italy. https://sowebapp.ct.ingv.it/oldweb/Report/WKRVGALT20090504.pdf. Accessed 8 Jul 2024

Cristaldi A (2009b) Rapporto sull'evento esplosivo dello Stromboli del giorno 08/11/2009 ripreso dalle telecamere di sorveglianza. Internal report no. UFVG2009/085, INGV, Sezione di Catania, Italy. https://www.ct.ingv.it/dmdocuments/CronologiaeventodelOSNovembre2009_01.pdf. Accessed 8 Jul 2024

Costa F, Shea T, Ubide T (2020) Diffusion chronometry and the timescales of magmatic processes. Nat Rev Earth Environ 1:201–214. https://doi.org/10.1038/s43017-020-0038-x

De Campos CP, Perugini D, Ertel-Ingrisch W, Dingwell DB, Poli G (2011) Enhancement of magma mixing efficiency by chaotic dynamics: an experimental study. Contrib Mineral Petrol 161:863–881. https://doi.org/10.1007/s00410-010-0569-0

Di Carlo I, Pichavant M, Rotolo SG, Scaillet B (2006) Experimental crystallization of a high-K arc basalt: the golden pumice, Stromboli volcano (Italy). J Petrol 47:1317–1343. https://doi.org/10.1093/petrology/egl011

D'Oriano C, Bertagnini A, Pompilio M (2011) Ash erupted during normal activity at Stromboli (Aeolian Islands, Italy) raises questions on how the feeding system works. Bull Volcanol 73:471–477. https://doi.org/10.1007/s00445-010-0425-0

Ding S, Plank T, Wallace PJ, Rasmussen DJ (2023) Sulfur_X: a model of sulfur degassing during magma ascent. Geochem Geophys Geosyst 24:e2022GC010552. https://doi.org/10.1029/2022GC010552

Dixon JE, Stolper EM (1995) An experimental study of water and carbon dioxide solubilities in mid-ocean ridge basaltic liquids. Part II: applications to degassing. J Petrol 36:1633–1646. https://doi.org/10.1093/oxfordjournals.petrology.a037268

Di Stefano F, Mollo S, Ubide T, Petrone CM, Caulfield J, Scarlato P, Nazzari M, Andronico D, Del Bello E (2020) Mush cannibalism and disruption recorded by clinopyroxene phenocrysts at Stromboli volcano: new insights from recent 2003–2017 activity. Lithos 105440. https://doi.org/10.1016/j.lithos.2020.105440

Edmonds M, Liu E, Cashman K (2022) Open-vent volcanoes fuelled by depth-integrated magma degassing. Bull Volcanol 84:28. https://doi.org/10.1007/s00445-021-01522-8

Francalanci L, Barbieri M, Manetti P, Peccerillo A, Tolomeo L (1988) Sr isotopic systematics in volcanic rocks from the island of Stromboli, Italy (Aeolian Arc). Chem Geol Isot Geoscience Section 73:109–124. https://doi.org/10.1016/0168-9622(88)90010-3

Francalanci L, Manetti P, Peccerillo A (1989) Volcanological and magmatological evolution of Stromboli volcano (Aeolian Islands): the roles of fractional crystallization, magma mixing, crustal contamination and source heterogeneity. Bull Volcanol 51:355–378. https://doi.org/10.1007/BF01056897

Francalanci L, Tommasini S, Conticelli S (2004) The volcanic activity of Stromboli in the 1906–1998 AD period: mineralogical, geochemical and isotope data relevant to the understanding of the plumbing system. J Volcanol Geotherm Res 131:179–211. https://doi.org/10.1016/S0377-0273(03)00362-7

Francalanci L, Davies GR, Lustenhouwer WIM, Tommasini S, Mason PR, Conticelli S (2005) Intra-grain Sr isotope evidence for crystal recycling and multiple magma reservoirs in the recent activity of Stromboli volcano, Southern Italy. J Petrol 46:1997–2021. https://doi.org/10.1093/petrology/egi045

Francalanci L, Avanzinelli R, Nardini I, Tiepolo M, Davidson JP, Vannucci R (2012) Crystal recycling in the steady-state system of the active Stromboli volcano: a 2.5-ka story inferred from in situ Sr-isotope and trace element data. Contrib Mineral Petrol 163:109–131. https://doi.org/10.1007/s00410-011-0661-0

Genco R, Ripepe M (2010) Inflation-deflation cycles revealed by tilt and seismic records at Stromboli volcano. Geophys Res Lett. https://doi.org/10.1029/2010GL042925

Ghiorso M, Gualda G (2015) An H2O–CO2 mixed fluid saturation model compatible with rhyolite-MELTS. Contrib Mineral Petrol 169:1–30. https://doi.org/10.1007/s00410-015-1141-8

Giordano G, De Astis G (2021) The summer 2019 basaltic vulcanian eruptions (paroxysms) of Stromboli. Bull Volcanol 83:1–27. https://doi.org/10.1007/s00445-020-01423-2

Girona T, Costa F (2013) DIPRA: a user-friendly program to model multi-element diffusion in olivine with applications to timescales of magmatic processes. Geochem Geophys Geosyst 14:422–431. https://doi.org/10.1029/2012GC004427

Hartley ME, Maclennan J, Edmonds M, Thordarson T (2014) Reconstructing the deep CO_2 degassing behaviour of large basaltic fissure eruptions. Earth Planet Sci Lett 393:120–131. https://doi.org/10.1016/j.epsl.2014.02.031

Houghton BF, Gonnermann HM (2008) Basaltic explosive volcanism: constraints from deposits and models. Geochem 68:117–140. https://doi.org/10.1016/j.chemer.2008.04.002

Iacono-Marziano G, Morizet Y, Trong E, Gaillard F (2012) New experimental data and semi-empirical parameterization of H_2O-CO_2 solubility in mafic melts. Geochim Cosmochim Acta 97:1–23. https://doi.org/10.1016/j.gca.2012.08.035

Iacovino K, Matthews S, Wieser PE, Moore GM, Bégué F (2021) VESIcal part I: an open-source thermodynamic model engine for mixed volatile (H_2O-CO_2) solubility in silicate melts. Earth Space Sci 8:e2020EA001584. https://doi.org/10.1029/2020EA001584

Kelfoun K, Harris A, Bontemps M, Labazuy P, Chausse F, Ripepe M, Donnadieu F (2020) A method for 3D reconstruction of volcanic bomb trajectories. Bull Volcanol 82:34. https://doi.org/10.1007/s00445-020-1372-z

Landi P, Métrich N, Bertagnini A, Rosi M (2004) Dynamics of magma mixing and degassing recorded in plagioclase at Stromboli (Aeolian Archipelago, Italy). Contrib Mineral Petrol 147:213–227. https://doi.org/10.1007/s00410-004-0555-5

Landi P, Métrich N, Bertagnini A, Rosi M (2008) Recycling and "rehydration" of degassed magma inducing transient dissolution/crystallization events at Stromboli (Italy). J Volcanol Geotherm Res 174:325–336. https://doi.org/10.1016/j.jvolgeores.2008.02.013

La Felice S, Landi P (2011) The 2009 paroxysmal explosions at Stromboli (Italy): magma mixing and eruption dynamics. Bull Volcanol 73:1147–1154. https://doi.org/10.1007/s00445-011-0502-z

Landi P, Corsaro RA, Francalanci L, Civetta L, Miraglia L, Pompilio M, Tesoro R (2009) Magma dynamics during the 2007 Stromboli eruption (Aeolian Islands, Italy): mineralogical, geochemical and isotopic data. J Volcanol Geotherm Res 182:255–268. https://doi.org/10.1016/j.jvolgeores.2008.11.010

Landi P, D'Oriano C, Petrelli M, Nazzari M, Andronico D (2022) Inferences on the magmatic plumbing system at Stromboli volcano (Italy) from trace element geochemistry of matrix glasses and minerals in different types of explosive eruptions. Contrib Mineral Petrol 177:96. https://doi.org/10.1007/s00410-022-01962-1

Lerner AH, Sublett DM Jr., Wallace PJ, Cauley C, Bodnar RJ (2024) Insights into magma storage depths and eruption controls at Kīlauea Volcano during explosive and effusive periods of the

past 500 years based on melt and fluid inclusions. Earth Planet Sci Lett 628:118579. https://doi.org/10.1016/j.epsl.2024.118579
Lesne P, Kohn SC, Blundy J, Witham F, Botcharnikov RE, Behrens H (2011) Experimental simulation of closed-system degassing in the system basalt–H O–CO –S–Cl. J Petrol 52(9):1737–1762. https://doi.org/10.1093/petrology/egr027
Lowenstern JB (1995) Applications of silicate-melt inclusions to the study of magmatic volatiles. Magmas, Fluids and Ore Deposits 23:71–99
LGS – Università degli Studi di Firenze (n.d.) Bulletins available online: https://lgs.geo.unifi.it/bulletins/. Accessed 8 Jan 2025
Maclennan J (2017) Bubble formation and decrepitation control the CO_2 content of olivine-hosted melt inclusions. Geochem Geophys Geosyst 18(2):597–616. https://doi.org/10.1002/2016GC006633
Métrich N, Wallace PJ (2008) Volatile abundances in basaltic magmas and their degassing paths tracked by melt inclusions. Rev Mineral Geochem 69:363–402. https://doi.org/10.2138/rmg.2008.69.10
Métrich N, Bertagnini A, Landi P, Rosi M (2001) Crystallization driven by decompression and water loss at Stromboli volcano (Aeolian Islands, Italy). J Petrol 42:1471–1490. https://doi.org/10.1093/petrology/42.8.1471
Métrich N, Bertagnini A, Landi P, Rosi M, Belhadj O (2005) Triggering mechanism at the origin of paroxysms at Stromboli (Aeolian Archipelago, Italy): the 5 April 2003 eruption. Geophys Res Lett. https://doi.org/10.1029/2004GL022257
Métrich N, Bertagnini A, Di Muro A (2010) Conditions of magma storage, degassing and ascent at Stromboli: new insights into the volcano plumbing system with inferences on the eruptive dynamics. J Petrol 51:603–626. https://doi.org/10.1093/petrology/egp083
Métrich N, Bertagnini A, Pistolesi M (2021) Paroxysms at Stromboli volcano (Italy): source, genesis and dynamics. Front Earth Sci 9:593339. https://doi.org/10.3389/feart.2021.593339
Moore LR, Gazel E, Tuohy R, Lloyd AS, Esposito R, Steele-MacInnis M, Hauri EK, Wallace PJ, Plank T, Bodnar RJ (2015) Bubbles matter: an assessment of the contribution of vapor bubbles to melt inclusion volatile budgets. Am Mineral 100(4):806–823. https://doi.org/10.2138/am-2015-5036
Newman S, Lowenstern JB (2002) Volatilecalc: a silicate melt-H_2O-CO_2 solution model written in visual basic for excel. Comput Geosci 28:597–604. https://doi.org/10.1016/S0098-3004(01)00081-4
Nolesini T, Di Traglia F, Ventisette CD, Moretti S, Casagli N (2013) Deformations and slope instability on Stromboli volcano: integration of GBInSAR data and analog modeling. Geomorphology 180:242–254. https://doi.org/10.1016/j.geomorph.2012.10.014
Patanè D, De Gori P, Cocina O, Zuccarello L, Garcia-Yeguas A, Castellano M, D'Alessandro A, Sgroi T (2017) The shallow magma chamber of Stromboli Volcano (Italy). Geophys Res Lett 44:6589–6596. https://doi.org/10.1002/2017GL073008
Perugini D, Poli G, Mazzuoli R (2003) Chaotic advection, fractals and diffusion during mixing of magmas: evidence from lava flows. J Volcanol Geotherm Res 124:255–279. https://doi.org/10.1016/j.lithos.2004.04.039
Petrone CM, Mollo S, Gertisser R, Buret Y, Scarlato P, Del Bello E, Andronico D, Ellis B, Pontesilli A, De Astis G, Giacomoni PP, Coltorti M, Reagan M (2022) Magma recharge and mush rejuvenation drive paroxysmal activity at Stromboli volcano. Nat Commun 13:7717. https://doi.org/10.1038/s41467-022-35405-z
Phillips JC, Woods AW (2001) Bubble plumes generated during recharge of basaltic magma reservoirs. Earth Planet Sci Lett 186:297–309. https://doi.org/10.1016/S0012-821X(01)00221-7
Pichavant M, Di Carlo I, Le Gac Y, Rotolo SG, Scaillet B (2009) Experimental constraints on the deep magma feeding system at Stromboli volcano, Italy. J Petrol 50:601–624. https://doi.org/10.1093/petrology/egp014
Pichavant M, Pompilio M, D'Oriano C, Di Carlo I (2011) Petrography, mineralogy and geochemistry of a primitive pumice from Stromboli: implications for the deep feeding system. Eur J Mineral 23:499–517. https://doi.org/10.1127/0935-1221/2011/0023-2109
Pichavant M, Di Carlo I, Pompilio M, Le Gall N (2022) Timescales and mechanisms of paroxysm initiation at Stromboli volcano, Aeolian Islands, Italy. Bull Volcanol 84:36. https://doi.org/10.1007/s00445-022-01545-9
Pioli L, Pistolesi M, Rosi M (2014) Transient explosions at open-vent volcanoes: the case of Stromboli (Italy). Geology 42:863–866. https://doi.org/10.1130/G35844.1
Pistolesi M, Delle Donne D, Pioli L, Rosi M, Ripepe M (2011) The 15 march 2007 explosive crisis at Stromboli volcano, Italy: assessing physical parameters through a multidisciplinary approach. J Geophys Res. https://doi.org/10.1029/2011JB008527
Ponte G (1919) La catastrofica esplosione dello Stromboli. R Accad Naz Lincei 28:89–94
Portnyagin M, Almeev R, Matveev S, Holtz F (2008) Experimental evidence for rapid water exchange between melt inclusions in olivine and host magma. Earth Planet Sci Lett 272:541–552. https://doi.org/10.1016/j.epsl.2008.05.020
Putirka KD, Perfit M, Ryerson FJ, Jackson MG (2007) Ambient and excess mantle temperatures, olivine thermometry, and active vs. passive upwelling. Chem Geol 241:177–206. https://doi.org/10.1016/j.chemgeo.2007.01.014
Rasmussen DJ, Plank TA, Wallace PJ, Newcombe ME, Lowenstern JB (2020) Vapor-bubble growth in olivine-hosted melt inclusions. Am Mineral 105:1898–1919. https://doi.org/10.2138/am-2020-7377
Ripepe M, Lacanna G, Pistolesi M, Silengo MC, Aiuppa A, Laiolo M, Delle Donne D (2021) Ground deformation reveals the scale-invariant conduit dynamics driving explosive basaltic eruptions. Nat Commun 12:1683. https://doi.org/10.1038/s41467-021-21722-2
Ripepe M, Donne DD, Harris A, Marchetti E, Ulivieri G (2008) Dynamics of Strombolian activity. Washington DC Am Geophys Union Geophys Monograph Ser 182:39–48. https://doi.org/10.1029/182GM05
Rittmann A (1931) Der ausbruch des Stromboli am 11 September 1930. Z Vulkanol 14:47–77
Robidoux P, Frezzotti ML, Hauri EH, Aiuppa A (2018) Shrinkage bubbles: the C-O–H–S magmatic fluid system at San Cristóbal volcano. J Petrol 59(11):2093–2122. https://doi.org/10.1093/petrology/egy092
Rose-Koga EF, Bouvier AS, Gaetani GA, Wallace PJ, Allison CM, Andrys JA et al (2021) Silicate melt inclusions in the new millennium: a review of recommended practices for preparation, analysis, and data presentation. Chem Geol 570:120145. https://doi.org/10.1016/j.chemgeo.2021.120145
Rosi M, Bertagnini A, Harris AJL, Pioli L, Pistolesi M, Ripepe M (2006) A case history of paroxysmal explosion at Stromboli: timing and dynamics of the April 5, 2003 event. Earth Planet Sci Lett 243:594–606. https://doi.org/10.1016/j.epsl.2006.01.035
Rosi M, Pistolesi M, Bertagnini A, Landi P, Pompilio M, Di Roberto A (2013) Chapter 14 Stromboli volcano, Aeolian Islands (Italy): present eruptive activity and hazards. Geological Society, London, Memoirs 37:473–490. https://doi.org/10.1144/M37.14
Shea T, Costa F, Krimer D, Hammer JE (2015) Accuracy of timescales retrieved from diffusion modeling in olivine: a 3D perspective. Am Mineral 100(10):2026–2042. https://doi.org/10.2138/am-2015-5163
Shishkina TA, Botcharnikov RE, Holtz F, Almeev RR, Jazwa AM, Jakubiak AA (2014) Compositional and pressure effects on the

solubility of H_2O and CO_2 in mafic melts. Chem Geol 388:112–129. https://doi.org/10.1016/j.chemgeo.2014.09.001

Sobolev VS, Kostyuk VP (1975) Magmatic crystallization based on a study of melt inclusions. Fluid Inclus Res 9:182–253

Steele-MacInnis M, Esposito R, Moore LR, Hartley ME (2017) Heterogeneously entrapped, vapor-rich melt inclusions record pre-eruptive magmatic volatile contents. Contrib Mineral Petrol 172(4):18. https://doi.org/10.1007/s00410-017-1343-3

Streck MJ (2008) Mineral textures and zoning as evidence for open system processes. Rev Mineral Geochem 69:595–622. https://doi.org/10.2138/rmg.2008.69.15

Taddeucci J, Scarlato P, Capponi A, Del Bello E, Cimarelli C, Palladino DM, Kueppers U (2012) High-speed imaging of Strombolian explosions: the ejection velocity of pyroclasts. Geophys Res Lett. https://doi.org/10.1029/2011GL050404

Toplis MJ (2005) The thermodynamics of iron and magnesium partitioning between olivine and liquid: criteria for assessing and predicting equilibrium in natural and experimental systems. Contrib Mineral Petrol 149:22–39. https://doi.org/10.1007/s00410-004-0629-4

Tucker JM, Hauri EH, Pietruszka AJ, Garcia MO, Marske JP, Trusdell FA (2019) A high carbon content of the Hawaiian mantle from olivine-hosted melt inclusions. Geochim Cosmochim Acta 254:156–172. https://doi.org/10.1016/j.gca.2019.04.001

Vergniolle S (2024) Origin of basaltic subplinian eruption at Shishaldin volcano (Alaska): a vigorously degassing magma reservoir hosting small bubbles. Journal of Geophysical Research: Solid Earth 129:e2023JB028161. https://doi.org/10.1029/2023JB028161

Vergniolle S, Métrich N (2021) Open-vent volcanoes: a preface to the special issue. Bull Volcanol 83:1–5. https://doi.org/10.1007/s00445-021-01454-3

Voloschina M, Métrich N, Bertagnini A, Marianelli P, Aiuppa A, Ripepe M, Pistolesi M (2023) Explosive eruptions at Stromboli volcano (Italy): a comprehensive geochemical view on magma sources and intensity range. Bull Volcanol 85:34. https://doi.org/10.1007/s00445-023-01647-y

Wallace PJ, Plank T, Bodnar RJ, Gaetani GA, Shea T (2021) Olivine-hosted melt inclusions: a microscopic perspective on a complex magmatic world. Ann Rev Earth Planet Sci 49:465–494. https://doi.org/10.1146/annurev-earth-082420-060506

Wallace PJ, Kamenetsky VS, Cervantes P (2015a) Melt inclusion CO_2 contents, pressures of olivine crystallization, and the problem of shrinkage bubbles. Am Mineral 100:787–794. https://doi.org/10.2138/am-2015-5029

Wallace PJ, Plank T, Edmonds M, Hauri EH (2015b) Volatiles in magmas. In: The encyclopedia of volcanoes, pp 163–183. Academic Press. https://doi.org/10.1016/B978-0-12-385938-9.00007-9

Wieser PE, Lamadrid H, Maclennan J, Edmonds M, Matthews S, Iacovino K, Jenner FE, Gansecki C, Trusdell F, Lee RL, Ilyinskaya E (2021) Reconstructing magma storage depths for the 2018 Kīlauean eruption from melt inclusion CO2 contents: the importance of vapor bubbles. Geochem Geophys Geosyst 22(2):e2020GC009364. https://doi.org/10.1029/2020GC009364